

Extended validation and evaluation of the OLCI-SLSTR Synergy aerosol product (SY_2_AOD) on Sentinel-3

Larisa Sogacheva¹, Matthieu Denisselle², Pekka Kolmonen¹, Timo H. Virtanen¹, Peter North³, Claire
5 Henocq², Silvia Scifoni⁴ and Steffen Dransfeld⁵

¹ Finish Meteorological Institute, Climate Programme, Helsinki, 00540, Finland

² ACRI-ST, Sophia-Antipolis, 06410, France

³ Global Environmental Modelling and Earth Observation (GEMEO), Dept. of Geography, Swansea University, SA28PP, UK

⁴ Serco Italia SpA for European Space Agency (ESA), European Space Research Institute (ESRIN), 00044 Frascati, Italy.

10 ⁵ European Space Agency (ESA), European Space Research Institute (ESRIN), Frascati, Italy

Correspondence to: Larisa Sogacheva (larisa.sogacheva@fmi.fi)

Abstract

We present the first extended validation of a new synergy global aerosol product (SY_2_AOD) which is based on synergistic
15 use of data from the Ocean and Land Color Instrument (OLCI), and the Sea and Land Surface Temperature Radiometer
(SLSTR) sensors onboard the Copernicus Sentinel-3A (S3A) and Sentinel-3B (S3B) satellites. Validation covers period from
14 January 2020 to 30 September 2021. Several approaches, including statistical analysis, time series analysis, comparison
with similar aerosol products from the other spaceborne sensor Moderate Resolution Imaging Spectroradiometer (MODIS),
were applied for validation and evaluation of S3A and S3B SY_2 aerosol products, including Aerosol Optical Depth (AOD)
20 provided at different wavelengths, AOD pixel level uncertainties, Fine Mode AOD and Angström exponent.

Over ocean, the performance of SY_2 AOD (syAOD) retrieved at 550 nm is good: for S3A and S3B respectively, Pearson
correlation coefficients with the Maritime Aerosol Network (MAN) component of the AEROSOL ROBOTIC NETWORK
(AERONET) are 0.88 and 0.85; 88.6% and 89.5% of pixels fit into MODIS Error Envelope (EE) of $\pm 0.05 \pm 0.2 \times \text{AOD}$.

Over land, correlation coefficients with AERONET AOD (aAOD) are 0.60 and 0.63 for S3A and S3B respectively; 51.4%
25 and 57.9% of pixels fit into MODIS EE. Reduced performance over land is expected since the surface reflectance and angular
distribution of scattering is higher and more difficult to predict over land than over ocean. The results are affected by a large
number of outliers.

Evaluation of the per-retrieval uncertainty with χ^2 test indicates that syAOD prognostic uncertainties (PU) are slightly
underestimated ($\chi^2 = 3.1$); if outliers are removed, PU describes well the syAOD error ($\chi^2 = 1.6$).

30 The regional analysis of the Angström exponent, which relates to the aerosol size distribution, shows spatial correlation with
expected sources. For 40% of the matchups with AERONET in the Northern Hemisphere (NH), and for 60% of the matchups
in the Southern Hemisphere (SH), which fit into the AE size range of [1 1.8], an offset between SY_2 AE (syAE) and

AERONET AE (aAE) is within ± 0.25 . General overestimation of low (< 0.5) syAE and underestimation of high (> 1.8) syAE is resulting in high (0.94, globally) overall bias.

35 Good agreement (bias < 0.03) was observed between Sy_2 Fine Mode AOD (syFMAOD) and AERONET Fine mode AOD (aFMAOD) for aFMAOD < 1 . At aFMAOD > 1 , syFMAOD is considerably underestimated (by 0.3-0.5 in different aFMAOD ranges) in the NH. In the SH, only few aFMAOD values above 1 are measured. Fine Mode Fraction (FMF) in the SY_2 AOD product (syFMF) in the range of [0 0.7] is overestimated; positive offset of 0.3-0.5 for low (< 0.25) FMF is gradually decreasing. Differences between the annual/ seasonal AOD values from SY_2 and MODIS (mod) Dark Target and Deep blue products are
40 within 0.02 for the study area [30°S-60°N, 80°W-45°E]. The agreement is better over ocean; however, difference up to 0.6 exists between syFMF and modFMF. Over bright land surface (Saharan desert) the difference in AOD between two products is highest (up to 0.11); the sign of the difference varies over time and space.

For both S3A and S3B AOD products, validation statistics are often slightly better in the Southern Hemisphere. In general, the performance of S3B is slightly better.

45 1 Introduction

The concern about climate change (e.g., Bergquist and Warshaw, 2019) along with a willingness to reduce its effects (e.g., Leiserowitz et al., 2020; Hoffmann et al., 2022) are of growing interest during the past decades. Global models introduce different scenarios for climate change (Arbor et al., 2021; Meehl et al., 2007), which are often based on the historical records and trends. Satellite data, including aerosols, provide unique global data on the Earth's surface and atmosphere; they are
50 assimilated into global and regional models (Khaki et al., 2020; Eyre et al., 2022) and used for model evaluation (Gliß et al., 2021).

Product quality depends on instrument specifications and applicability of the retrieval approaches. Despite having an advantage in coverage over ground-based products, satellite products often concede lower, compared with ground-based measurements, quality. However, with the fast development of the space-born instruments, including improved quality of onboard instruments
55 and increased temporal and spatial coverage (CEOS, 2017; Dubovik et al., 2021), and on the other hand with improved access to satellite products (Borowitz, 2018) following open access policy (Harris and Bauman, 2015; Olbrich, 2018) and standardisation of satellite data (Loew et al., 2017), the contribution of the space-borne measurements in climate studies is gradually increasing.

Calibration and validation (cal/val) are essential to characterise the quality of the performance of a mission
60 (<https://earth.esa.int/eogateway/documents/20142/1564943/Sentinel-3-Calibration-and-Validation-Plan.pdf>, last access 14 February 2022). Calibration tasks include pre-launch and in-flight calibrations and characterisation, as well as comprehensive verification of Level-1 data processors. For optical missions, radiometric, spectral, and geometric stability are subjects for investigation.

Validation is a part of a cal/val activity. In the context of remote sensing, validation refers to the process of quantifying the accuracy of satellite retrieved products by assessing the uncertainty of the derived products by analytical comparison to reference data, which is presumed to represent the true value of an attribute. Validation shows the maturity of the satellite derived product and, thus, provides a conclusion on the mission success. Besides providing information about the product quality, validation may reveal a degradation of the instrument or potential drift (Julien and Sobrino, 2021). Validation results should be used in quality assurance reporting together with product details, calibration characterisation, retrieval algorithm description, and uncertainty characterisation.

Validation is a comparison against in-situ measurements, systematic and campaigns, and inter-comparison against other satellite data sources and/or models. Validation requires reference data with high reliability. Since the performance of a retrieval algorithm may vary in different conditions, validation also requires well-sampled coverage of useful ranges of measured values. Possible uncertainties of the product used as the “truth” must be considered. Since other satellite products and models may have their own biases, the inter-comparison against models and other satellite products is called evaluation. Changes in sensors and algorithms may be revealed if similar validation approaches are employed for different versions of products. Thus, common validation principles and approaches should be followed to allow the inter-comparison. General validation is product-specific, while detailed validation is instrument-specific. Validation requires an expertise on instrument, processing, and application, and a good understanding of limitations; thus general validation approaches have to be adapted considering specifications of particular products (e.g., temporal, spatial, radiometric resolutions).

An independent verification processing system is important. The purpose of validation is not only to show how good or bad the product is; issues explaining differences between product and reference data should be identified. Based on validation and evaluation results, recommendations on the product improvements can be provided to the product developers. Recommendations are important as they will help to identify conditions where an algorithm performance should be improved. Iterations on the product validation results with product developers, such as the round robin approach (Holzer-Popp et al, 2013), is a good example on how communication between validation team and product developers should be organised to better utilise validation results for an improvement of product quality.

In this paper we introduce global validation and evaluation results for the Synergy Aerosol Optical Depth (AOD) product, SY_2_AOD (North and Heckel, 2019), for the period from 14 January 2020 to 30 September 2021. The SY_2_AOD product is retrieved from spatially and temporally collocated data measured with two instruments, Sea and Land Surface Temperature Radiometer (SLSTR) and Ocean and Land Color Instrument (OLCI) onboard Sentinel-3 (S3A and S3B) satellites. The synergy retrieval algorithm has been originally developed for the retrieval of AOD from the Advanced Along-Track scanning Radiometer (AATSR) and MEdium-spectral Resolution Imaging Spectrometer (MERIS) (North et al., 2008) and further developed for the S3 instruments. The SY_2_AOD product is available from both S3A and S3B satellites. Extensive and systematic AOD validation against ground-based measurements and inter-comparison with Moderate Resolution Imaging Spectroradiometer (MODIS) AOD product were performed in the frame of the European Space Agency (ESA)

“ESA/Copernicus Space Component Validation for Land Surface Temperature, Aerosol Optical Depth and Water Vapour Sentinel-3 Products” (LAW, <https://law.acri-st.fr/home>, last access 10 January 2022).

The paper is structured as following. The SY₂ retrieval algorithm and SY₂_AOD product are introduced in Sect.2. In Sect. 3 we introduce a validation approach applied in the current study. An algorithm developed for extracting satellite and ground-based measurements matchups is explained in Sect.4. Reference validation products are introduced in Sect.4. AOD, AOD uncertainties, Fine mode AOD (FMAOD), Fine Mode Fraction (FMF), Angström exponent (AE) validation results with AERONET are shown in Sect. 6. AOD₅₅₀ validation results with SURFRAD and SKYNET are shown in the Supplement (Sections S1 and S2, respectively). Validation results over ocean are presented in Sect. 7. Inter-comparison of daily, monthly, seasonal, and annual SY-2 AOD and MODIS AOD products is shown in Sect.8. Validation results are summarised in Sect. 9.

2 SY₂ AOD product

2.1 Instrument description

OLCI and SLSTR L1b top-of-the-atmosphere (TOA) radiances were utilized in the SYNERGY algorithm for the retrieval of aerosol properties.

The Sentinel-3 OLCI (<https://sentinels.copernicus.eu/web/sentinel/technical-guides/sentinel-3-olci/olci-instrument>, last access 16 March 2022) is a push-broom imaging spectrometer with a swath width of 1270 km. It provides spatial sampling at 300 m with five cameras in 21 bands in the spectrum range of 0.4-1.2 μm .

The SLSTR instrument (<https://sentinels.copernicus.eu/web/sentinel/technical-guides/sentinel-3-slstr/instrument>, last access 16 March 2022) is a conical scanning imaging radiometer employing the along track scanning dual view technique. With the dual view scan (at near nadir and 55° oblique), measurements are taken at nine bands in the range of 0.55-12 μm covering the visible, shortwave infrared, and thermal infrared areas of the spectrum. The SLSTR spatial resolution is 500 m at nadir for visible and shortwave infrared bands and 1km at thermal infrared.

2.2 Algorithm description

The aim of the SYNERGY aerosol algorithm is to provide global aerosol optical depth and related aerosol properties for all cloud and ice-free regions of the Sentinel-3 combined OLCI / SLSTR instrument swaths. The SLSTR retrieval (ESA Aerosol CCI+ portal, <https://climate.esa.int/en/projects/aerosol/key-documents/>, Algorithm Theoretical Basis Document, last access: 25 February 2022) is of variable quality, with higher uncertainty in retrievals in the oblique backscattering direction. The motivation of combining the SLSTR with OLCI is to improve the SLSTR retrieval using additional spectral information from OLCI. The algorithm is derived originally from the aerosol retrieval algorithm developed by Swansea University under the ESA Aerosol CCI programme for the (A)ATSR and SLSTR instruments (North 2002; Bevan et al., 2012; Popp et al., 2016) but with further development to exploit the increased spectral sampling available from the OLCI instrument. This aims to

allow a more robust retrieval, but also to provide aerosol estimates over the full Sentinel-3 swath, whereas for the original algorithms using only SLSTR imagery, retrieval over land is only attempted for the regions where both nadir and oblique views are available. The key features of the algorithm are given here and are summarised in detail the SYN AOD Algorithm
130 Theoretical Basis Document (North and Heckel, 2019).

2.2.1 Pre-processing

The algorithm uses the L1c co-registered OLCI and SLSTR data product as input, projected on the OLCI grid. Co-registration is made based on the common 865 nm radiometric band. Over selected ground-control points, radiometric images of SLSTR 865 nm band are extracted and compared to the OLCI 865 nm acquisitions. The OLCI image is moved
135 around according to shift vectors and the cross-correlation with the fixed SLSTR window is calculated. The elements of the shift vectors at which a maximum in cross-correlation is reached determine the pixel deregistration between OLCI and SLSTR reference channel.

Over ocean, AOD is returned using the full swath of the Level 1c (L1c) product (1400 km), while over land the region covered by both nadir and oblique view (750km) is used for best quality retrieval, and aerosol retrieval is
140 also made outside of this region where both nadir-only SLSTR and OLCI is available (~1200 km). Beginning with the L1c product, pixels are flagged to screen cloud, snow ice or sun glint areas. In addition, all neighbouring pixels to cloud pixels are flagged to avoid edge effects. Pixels are grouped into ‘super-pixels’ formed by blocks of 15x15 pixels of the L1c SYN pixels at 300 m spatial resolution. Thus, a super-pixel represents a resolution of about 4.5 km x 4.5 km. The result is a super-pixel giving aggregated cloud-free TOA radiance for nadir and oblique view (if present) of the same surface location. The
145 inversion is carried out for all land and ocean super-pixels which are at least 50% free of cloud, ice and snow. Over ocean retrieval proceeds if either nadir or oblique super-pixels are valid, while over land both nadir and oblique must be valid for dual view retrieval, or nadir only for single view (spectral) retrieval.

2.2.2 Inversion to derive aerosol parameters

The basis of the algorithm is iterative non-linear optimisation to jointly retrieve aerosol optical depth at a reference wavelength
150 of 550nm, referred to as AOD_{550} , and Fine Mode Fraction (FMF) of AOD_{550} . Atmospheric radiative transfer is approximated as a Look-up Table (LUT) to relate top of atmosphere to surface reflectance, for a given estimate of aerosol parameters, water vapor, ozone and surface pressure. Over both land and ocean, the retrieval requires optimisation of a cost function expressing fit of derived surface reflectance to ocean or land models of reflectance. Several additional parameters are provided, derived from these properties, to provide information on spectral variation of AOD, and surface reflectance values intended as
155 diagnostics (see Sect.2.3 for details). Where a single viewing direction is used, the inversion is made over spectral bands in that direction only. This is normally the case outside the oblique view swath, where nadir only is used, but use of the oblique view alone also occurs over ocean where the nadir view is obscured by glint or cloud. Over ocean, only SLSTR channels (five

spectral bands, corresponding to S1 (554 nm); S2 (659 nm); S3 (865 nm); S5 (1613 nm) and S6 (2255 nm)) are taken into account in the aerosol retrieval. Over land, both sensors (including OLCI 442.5 nm spectral band) are considered.

160 A climatology of aerosol composition (Kinne et al., 2013; de Leeuw et al., 2015) is used to provide further information on the fine and coarse components (non-spherical vs spherical, single scattering albedo) and a prior estimate of fine mode fraction. We fit parameters for both AOD and FMF, which controls the spectral variation of AOD. Although AOD is parameterised by a single nominal wavelength (550 nm), all wavelengths of SLSTR, and additionally the 442.5 nm OLCI channel over land are used in this fitting. The SSA is constrained by climatology for the coarse and fine mode extremes separately and as a priori
165 information. The retrieval of FMF results in a SSA by interpolation between these extremes; however, this should be seen as a potential diagnostic for retrieval performance rather than a user product. Further constraints prevent unfeasible retrieval (e.g. negative AOD or surface reflectance). An estimate of the 1 standard deviation (std) error in AOD at 550 nm is derived from the second derivative (curvature) of the error surface near the optimal value.

Over ocean, a surface reflectance model gives a reflectance estimate determined from the wind speed and direction and using
170 the models of Cox and Munk (1954) for glint, Monahan and O'Muircheartaigh (1980) and Koepke (1984) for foam fraction and spectral reflectance, and Morel's case I water reflectance model dependent on pigment concentration (Morel, 1988). The ocean inversion uses bands from SLSTR only, using both views to invert if both are available, or a single view (either nadir or oblique) where one view is either obscured by cloud, is contaminated by glint, or lies in a swath region where only a single view is present. For land, the reflectance constraint is the result of fitting to separate angular and spectral parameterised models
175 (North, 2002; North et al., 2008; Davies and North, 2015; North and Heckel, 2019). Where the oblique SLSTR view is not available, only the spectral constraint is used, allowing AOD estimation over the full L1c swath over both land and ocean.

2.2.3 Post-processing

A final step is used to filter residual cloud contamination or other sources of poor retrieval. This is based on thresholding of local image standard deviation, discussed in Sogacheva et al., 2017. Over ocean, a final screening is also made on the quality
180 of model fit. Any AOD value outside the AOD valid range of [0, 4] is replaced by a 'fill' value 6.53. 'Clean-air' test is performed to recognise cases when an extensive rejection of low AOD values occurs in case of clean atmosphere, which often happens over dark surfaces. In case this test is positive, which is indicated in quality flags, a value of 0.04 is used.

During post-processing, further aerosol outputs are derived from the retrieved AOD₅₅₀ and FM AOD. This includes spectral variation of AOD, which is given using pre-computed look-up table from the retrieved FM AOD and aerosol mixture. The
185 Angström exponent is computed based on a pair of spectral AOD values. Here we choose 865 nm and 550 nm. A full set of quality flags is provided.

2.3 SY_2 AOD product description

Derived aerosol outputs include AOD, AOD uncertainty and single scattering albedo (each at 440 nm, 550 nm, 670 nm, 865 nm, 1610 nm), aerosol absorption optical depth, fine mode AOD, dust AOD (each at 550 nm) and Angström exponent (between

190 550 nm and 865 nm). The full list of derived aerosol outputs which are recorded in gridded NetCDF format at 4.5 km resolution, is shown in Table S1. Additionally for each super-pixel, information is provided giving time and location, solar/view geometry, cloud fraction, AOD retrieval quality flags, and retrieved surface reflectance for each waveband. Quality flags indicate which retrieval method was used, for example nadir-only or dual view, land/ocean algorithm and further indicators such as retrieval failure through negative AOD estimation or glint contamination.

195 **3 Validation approach**

The validation approach suggested for the European Space Agency (ESA) Climate Change Initiative (CCI) AOD product validation (ESA Aerosol CCI portal, <https://climate.esa.int/en/projects/aerosol/key-documents/>, Product Validation and Intercomparison Report, last access: 25 February 2022; de Leeuw et al., 2015) and currently used in ESA Aerosol CCI and Copernicus Climate Change Service C3S_312b_Lot2 projects was followed. A similar validation approach has been applied
200 and further developed in Sogacheva et al. (2018a, 2018b, 2020) for validation of the AATSR, MODIS and merged AOD products. The approach includes three main steps: i) match-up between satellite-retrieved AOD and ground-based measurements (Sect.4), ii) statistical tools application to the set of matchups to reveal the agreement between two products (Sect.6) and iii) analysis of the statistics. Different aspects of the validation and evaluation of various AOD products (Chu et al., 2002; Ichoku et al., 2002; Remer et al., 2005; Levy et al., 2013; Shi et al., 2013; Sayer et al., 2012a,b, 2013, 2018, 2019)
205 have been considered. Analysis of the AOD pixel-level provided uncertainties was performed based on the recommendations by Sayer et al. (2020) and considering best practices from the ESA Aerosol CCI.

Annual and seasonal validation was performed globally for all data. Furthermore, respective validations were made over selected areas, which represent different surface and aerosol types.

In the NH, the SLSTR oblique scan generally samples backscattered radiance, which has a weaker aerosol contribution than
210 the corresponding forward scattering sampled in the SH (e.g., https://www-cdn.eumetsat.int/files/2021-09/SARP_Report_Option_1_final.pdf, last access: 25 February 2022). This leads to reduced quality in AOD in the NH compared with SH for the SLSTR products, which has been revealed earlier (https://climate.esa.int/media/documents/Aerosol_cci_PVIR_v1.2_final.pdf, last access: 25 February 2022). For this reason, SY_2 AOD products from the NH and SH were validated separately.

215 syAOD₅₅₀ validation was performed for all available matchups and separately for groups of the matchups assorted based on prevailing aerosol types. Aerosol types were defined with AERONET AOD (aAOD) and AERONET AE (aAE) thresholds. Although these thresholds are subjective, we consider “background” aerosol to be cases where $aAOD_{550} < = 0.2$, “fine-dominated” with $aAOD_{550} > 0.2$ and $aAE > = 1$, and “coarse-dominated” with $aAOD_{550} > 0.2$ and $aAE < 1$ (e.g. Eck et al., 1999). This classification has also been used by e.g. Sayer et al. (2018) and Sogacheva et al. (2018a, b, 2020).

220 Another specification of the SY_2 AOD product is that the AOD retrieval has been performed with different retrieval approaches, depending on SLSTR and OLCI coverage and L1B data availability in different viewing angles (for details, see

Sect.2). Dual-view processor has been applied when SLSTR measurements from both views, nadir and oblique, were available. If measurements were available from one view only, the single view processor was applied to either nadir (over either land or ocean) or oblique view (over ocean or inland waters only). This specification of the product was considered in the current validation exercise.

4 Matchups extraction

A matchup is defined as the combination of simultaneous and spatially collocated satellite and ground-based measurements. Following Ichoku et al (2002), a macro pixel of 11x11 SY_2 AOD pixels (a surface of ca 50 km x 50 km) around each station was extracted at each overpass over a ground-based measurement station. All ground-based measurements were acquired in a time window of ± 30 minutes around the satellite crossing time were considered. Statistics such as number of measurements, mean, median, minimum, maximum and standard deviation computed over this time frame were included in the matchup files. All ground-based measurements were extracted from well-qualified networks introduced in Sect. 5.1 (AERONET), Sect. 5.2 (MAN) and in the supplement (SURFRAD, SKYNET); no additional quality control check has been performed for the reference data. On the contrary, all satellite extractions included all quality flags and contextual parameters presents in the Sentinel-3 operational products. Satellite extractions were created automatically for each station, at each overpass, and centred on the station location. They were then associated with relevant ground-based measurements when these data were available and validated.

“Empty” matchups, i.e., when the whole satellite extraction is associated with a fill value for AOD, were not filtered out from the database, except in case of operational issues in the Sentinel-3 instruments. As these fill values were mainly due to cloud contamination or aerosol retrieval failure, they may provide information about the performance of, e.g., cloud screening in the SY_2 algorithm and were therefore relevant to validation objective.

A free access (upon subscription) to this matchups database has been provided on the ESA LAW web portal (<https://law.acri-st.fr/home>, last access 10 January 2022).

To explore the performance of different processors, four separate datasets were created and validated separately. The first dataset (called ‘all’ in the following) consists of all available data, regardless of which processor was used. The second dataset (‘dual’) contains data retrieved with the dual view processor. The third (‘singleN’) and fourth (‘singleO’) dataset are created using the single view processors applied to nadir or oblique views, respectively. The total number of matchups from dual, singleN and singleO groups is higher than the total number of ‘all’ matchups, because in 11x11 pixels area around reference ground-based measurement there could have been pixels retrieved with different processors (e.g., dual and singleN). In that case we have two matchups (one for dual group and one for single group) for the same spatial-temporal window. If the group not mentioned specifically (‘dual’, ‘singleN’ or ‘singleO’, in the text or in the figure), results are shown and discussed for the group ‘all’.

5 Reference datasets

5.1 AERONET

255 The AERONET is a federation of ground-based remote sensing aerosol networks (<https://aeronet.gsfc.nasa.gov/>, last access: 25 February 2022). For more than 25 years, AERONET has provided a long-term, continuous, and readily accessible public domain database of aerosol optical, microphysical, and radiative properties for aerosol research and characterization, validation of satellite retrievals, and synergism with other databases. An extensive description of the AERONET sites, procedures and data provided is available from the AERONET web site and in (Holben et al., 1988, Giles et al., 2019).

260 Ground-based sun photometers directly observe the attenuation of solar radiation without interference from land surface reflections. They provide accurate measurements of AOD with uncertainty ~ 0.01 – 0.02 (Eck et al., 1999) in the spectral range of 340–1640 nm.

For the AOD validation, AERONET version 3 data (Giles et al., 2019) – automated near-real-time quality control algorithm with improved cloud screening for Sun photometer aerosol optical depth (AOD) measurements – has been utilized. Version 3
265 AOD data are computed for three data quality levels: Level 1.0 (unscreened), Level 1.5 (cloud-screened and quality controlled), and Level 2.0 (quality-assured). The Level 2.0 AOD quality-assured dataset is now available within a month after post-field calibration, reducing the lag time from up to several months.

Since AERONET is a network of ground-based sun-photometers, and while some of the AERONET stations are in the coastal land areas and on the islands, open ocean is poorly covered with AERONET. Thus, another available network (see Sect 5.2)
270 is used for validation of AOD retrieved over open ocean.

5.2 MAN

The Maritime Aerosol Network (MAN) component of AERONET provides ship-borne AOD measurements from the Microtops II sun photometers (Smirnov et al., 2009). These data provide an alternative to observations from islands as well as establish validation points for satellite and aerosol transport models. Since 2004, these instruments have been deployed
275 periodically on ships providing an opportunity for monitoring aerosol properties over the world oceans.

The Microtops II Sun photometer is a handheld device specifically designed to measure columnar optical depth and water vapor content (Morys et al., 2001). The direct Sun measurements are acquired in five spectral channels within the spectral range 340–1020 nm. The bandwidths of the interference filters vary from 2 to 4 nm (UV channels) to 10 nm for visible and near-infrared channels. The MAN instruments are calibrated against the same reference instruments as utilized in AERONET.

280 The estimated uncertainty of the optical depth in each channel does not exceed ± 0.02 , which is slightly higher than the uncertainty of the AERONET field (not master) instruments as shown by Smirnov et al. (2006).

Comparison of MAN and AERONET AOD data does not show any particular bias for AERONET and MAN, although a visible cluster of points above the 1:1 line was acquired in a highly variable dust outbreak conditions west of Africa in the North Atlantic (Smirnov et al., 2011).

Moderate Resolution Imaging Spectroradiometer (MODIS) was launched onboard Terra in 1999. It has a wide spectral range from $0.41\mu\text{m}$ to $14.5\mu\text{m}$, broad swath of 2330 km, and relatively fine spatial resolution of 250 m to 1 km (Levy et al., 2013). The local equator crossing times for MODIS onboard Terra is 10:30.

In this study, the Level 2 combined Dark Target and Deep Blue (DT&DB) AOD product (MOD04_L2) from MODIS Terra collection C6.1 was utilized, which is characterized by good quality and better than Dark Target or Deep Blues coverage alone (Wei et al., 2019).

6 Validation with AERONET

The AERONET network does not cover the globe evenly. The location of AERONET stations and number of S3A collocations per AERONET station utilized in the validation exercise are shown in Figure 1. For S3B, the number of matchups is similar (slightly higher).

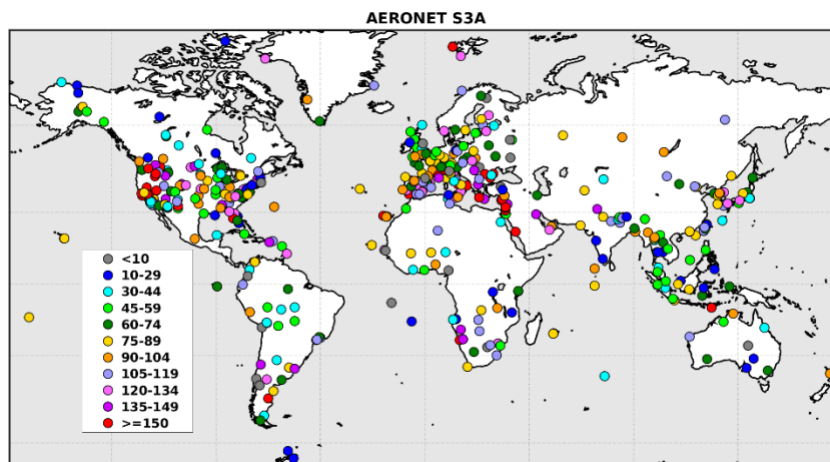


Figure 1: Location of the AERONET stations and number of matchups with S3A, per station (see legend) for the period 14 January 2020 to 30 September 2021.

In the exercise it was found that the validation results for S3A and S3B are, in general, similar (difference between results for S3A and S3B is less than 10% of S3A AOD). In this paper, validation results for S3A are shown in figures, while validation statistics for both S3A and S3B (shown as S3A/S3B) are summarised in tables and discussed.

6.1 AOD at 550nm

AERONET does not provide AOD at 550 nm (this dataset will be referred in the following as aAOD_{550}). AERONET AOD_{440} (aAOD_{440}) and AERONET Angström exponent for 440 nm and 870 nm ($\text{aAE}_{440,870}$) are used to calculate aAOD_{550} following the AOD spectral dependence feature (a power law relationship, Angström, 1929). However, aAOD_{440} is not measured at all

AERONET stations. For those stations, aAOD for another wavelength (400 nm or 500 nm) has been used to interpolate aAOD to 550 nm.

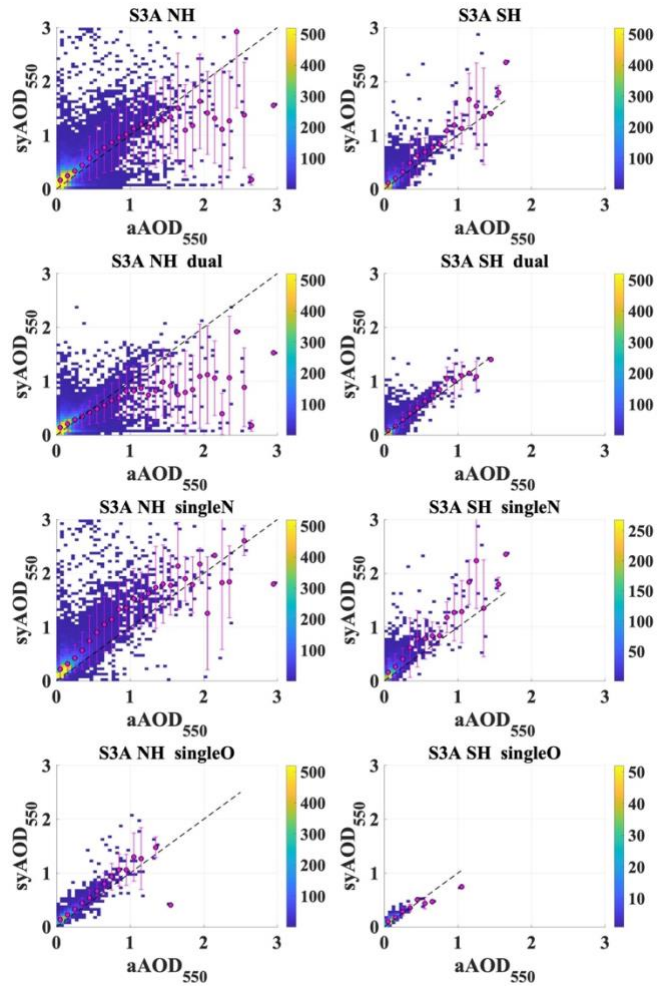
As shown in Figure 1, AERONET stations are not evenly distributed globally. For the study period, more than 85% of the matchups were from the NH. Thus, most of global results were strongly influenced by the results obtained for the NH. In case validation results are similar for the globe and the NH, results for the globe are not visualised. In case of a significant difference between the results for the globe and the NH, we show figures and discuss results for both. Validation statistics summarised in tables include results for the globe, NH, and SH.

6.1.1 Annual results

Scatter density plots for S3A SY_2 AOD₅₅₀ (syAOD₅₅₀, or syAOD) and corresponding AERONET AOD₅₅₀ (aAOD₅₅₀, or aAOD) for all matchups available for the NH and SH, including binned AOD offsets, are shown in Figure 2. For most of the matchups (91 %), syAOD is small (<0.4).

Validation statistics (number of points, N; percentage of matchups which fit into MODIS AOD error envelope (EE) defined as $\pm 0.05 \pm 0.2 \times \text{AOD}$ (Remer et al., 2013); percentage of matchups which satisfy Global Climate Observing System (GCOS) requirements of 0.03 or 10% of AOD (GCOS, 2016); Pearson correlation coefficient (R); root mean square (rms); standard deviation, std; bias and slope defined with linear regression (polynomial fit) applied to all available matchups) for S3A and S3B products are shown in Table 1.

A difference in the algorithm performance in the NH and SH is clear. For S3A, the fraction of matchups in the EE (70.8 %) and the fraction of matchups which satisfy GCOS requirements (43.0 %,.) are considerably higher in the SH (in the NH, 48.2 % and 20.5 % , respectively), but R (0.62) and rms (0.22) are only slightly better (in the NH, 0.6 and 0.28, respectively). For all matchups, validation statistics are better for S3B: in the SH, more matchups fit to the EE (74.6 %.), GCOS (44.9 %.), R (0.70) is higher, rms (0.15) is lower. In the NH, the difference between S3A and S3B is smaller.



330 **Figure 2:** Scatter density plots for S3A $syAOD_{550}$ and corresponding $aAOD_{550}$ for all, dual, singleN and singleO groups of matchups (panels top down) available over the NH (left panel) and SH (right panel). The filled magenta circles are the averaged $syAOD$ binned in 0.1 $aAOD$ intervals and the vertical lines on each circle represent the 1σ standard deviation of the fits.

335

Table 1 Validation statistics (number of points, N; percentage of matchups which fit into MODIS AOD error envelope, EE, defined as $\pm 0.05 \pm 0.2 \times \text{AOD}$; percentage of matchups which satisfy GCOS requirements (0.03 or 10% of AOD); correlation coefficient, R; root mean square, rms; standard deviation, σ ; bias and slope defined with linear regression applied to all available matchups) for S3A and S3B syAOD₅₅₀ products for the globe, NH and SH for the whole period for all matchups and for three groups of matchups, defined with the processor applied (dual, singleN, singleO).

group	area	N		EE, %		GCOS, %		R		rms		std		bias		slope	
		S3A	S3B	S3A	S3B	S3A	S3B	S3A	S3B	S3A	S3B	S3A	S3B	S3A	S3B	S3A	S3B
all	globe	38376	38829	51.4	57.9	23.8	27.7	0.60	0.63	0.28	0.24	0.001	0.001	0.12	0.10	0.89	0.87
	NH	32856	33240	48.2	55.1	20.5	24.8	0.60	0.62	0.28	0.25	0.001	0.001	0.13	0.11	0.86	0.85
	SH	5520	5589	70.8	74.6	43.0	44.9	0.62	0.70	0.22	0.15	0.003	0.002	0.04	0.04	1.19	1.06
dual	globe	25098	25796	57.9	61.9	29.1	32.1	0.61	0.64	0.19	0.18	0.001	0.001	0.11	0.09	0.62	0.65
	NH	21430	21989	54.2	59.0	25.4	29.3	0.60	0.62	0.20	0.19	0.001	0.001	0.12	0.10	0.58	0.62
	SH	3668	3807	79.3	78.7	50.5	48.3	0.79	0.78	0.12	0.12	0.002	0.002	0.02	0.02	1.07	1.03
singleN	globe	19986	19936	37.9	46.2	14.1	18.1	0.66	0.67	0.35	0.30	0.002	0.002	0.14	0.12	1.20	1.13
	NH	17114	17084	35.5	43.6	11.8	15.4	0.67	0.67	0.36	0.31	0.002	0.002	0.15	0.13	1.19	1.12
	SH	2872	2852	51.7	61.8	27.8	33.9	0.58	0.62	0.30	0.19	0.005	0.003	0.09	0.07	1.31	1.11
singleO	globe	5235	5396	57.7	54.9	20.4	18.3	0.90	0.90	0.11	0.11	0.001	0.001	0.06	0.07	1.12	1.07
	NH	4898	5027	56.2	52.8	18.5	16.0	0.90	0.90	0.11	0.11	0.001	0.001	0.06	0.07	1.12	1.07
	SH	337	369	80.4	82.7	48.7	50.4	0.85	0.88	0.06	0.06	0.003	0.002	0.05	0.03	0.83	1.07

340 In addition to the statistics shown in Table 1, we performed respective analysis for limited AOD ranges. For aAOD<1.5, syAOD validation statistics are slightly better than statistics for all aAOD ranges: bias is close to 0.1, slope is close to 1 for both S3A and S3B AOD products in the NH. For aAOD>1.5, bias is ca. 1.3 in the NH (where N is 127/125 for S3A/S3B, respectively). In the SH matchups available for S3B product are located close to the 1:1 line, however the number of matchups with aAOD>1.5 is small (N is 3/2) to calculate validation statistics.

345 Group (dual, singleN, singleO) analysis reveals that most of the low biased syAOD outliers were retrieved with the dual processor (Figure 2), while most of the high biased syAOD outliers were retrieved with the singleN processor. Total bias is smaller for the dual group globally, and in both NH and SH (Table 1). For aAOD<1.5, syAOD bias is close to 0 for the dual group; for the singleN group bias is higher than for all matchups and increasing with aAOD. Validation statistics are, in general, better in the SH (except for R for all the single groups). As for all matchups, validation statistics are slightly better for S3B.

350 Analysis of the binned (based on aAOD, bin size of 0.1) syAOD offsets to aAOD was carried out. For S3A (Figure 3), the dual group shows better performance. In this group, positive at low (<0.2) AOD offset is vanishing towards higher AOD and turns to negative at AOD>0.4. About 91 % of matchups fit to the AOD range of [0, 0.4]. In this AOD range, an offset is 0.03-0.05 higher in the NH compared with the SH. Offsets for the S3B in the same AOD range are lower (up to 0.03). Offsets for singleN and singleO groups are positive in the AOD range of [0, 1.2]. For high AOD, offsets are in general higher; however, less than
355 1.4% of the matchups fit to the range of aAOD>1.

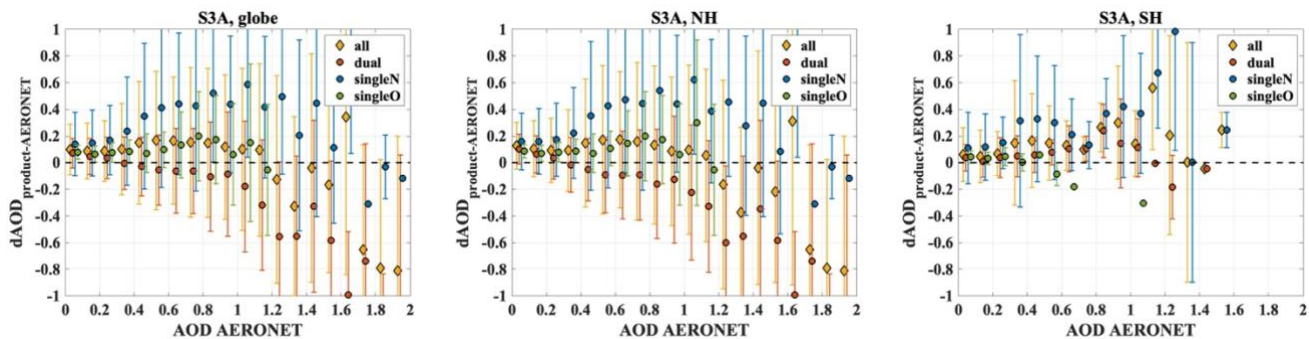


Figure 3: For S3A, binned in 0.1 aAOD intervals, syAOD offsets (dAOD) for the globe, the NH and SH (left to right) for all matchups, dual, singleN and singleO groups of matchups (yellow rhombus, red, green and blue dots, respectively, see legend)

For the aAOD binned on 0.1 intervals, the global difference (dAOD) between syAOD and aAOD represented with the median bias and dAOD standard deviation is shown in Figure 4 for all aerosol types (including background (aAOD \leq 0.2) AOD), fine-dominated and coarse-dominated AOD. Globally, background AOD (64% from all matchups) is overestimated by 0.04-0.06. Overestimation of fine-dominated matchups is increasing from 0.07 to 0.15 in the AOD range of 0.2-1.2 (34% of matchups). Overestimation for coarse-dominated matchups is about 0.05 for aAOD < 0.7; for aAOD of 0.7-0.9, an overestimation for coarse-dominated matchups is within the GCOS requirements of ± 0.03 dAOD. For aAOD > 1.2, dAOD is varying in the sign and in amplitude; however, the number of matchups in this size range is low (< 1%) and results are thus unstable. Fractions of the fine-dominated matchups per bin is 60-70% for aAOD in the range of 0.2-0.9 and more than 70% for aAOD > 0.9. Thus, binned offsets for all matchups follow closely offsets for fine-dominated matchups.

In the NH, the syAOD offset for the background matchups is ~ 0.07 ; in the SH the offset is lower (< 0.02). Binned offsets for the fine-dominated and coarse-dominated matchups in the NH are similar from those for the globe. In the SH, offsets of syAOD are higher for aAOD > 0.4, where the number of the matchups per bin is low (< 50).

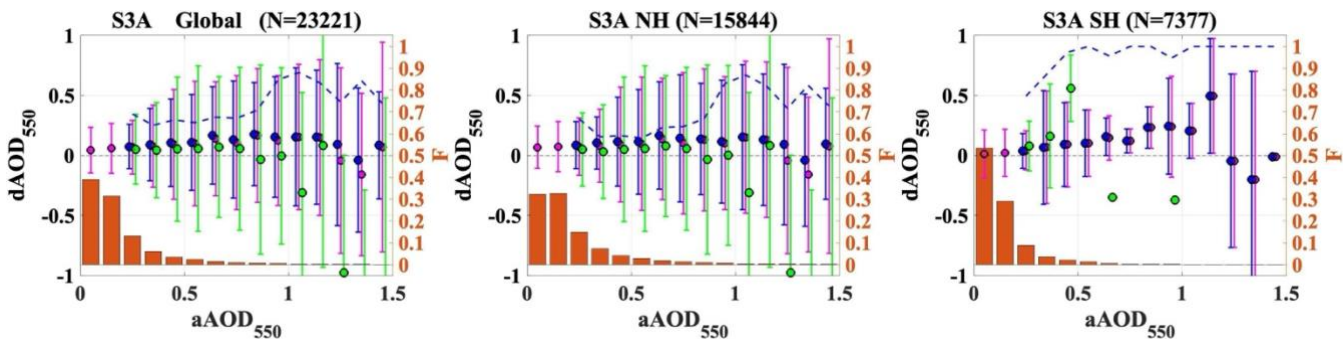


Figure 4: Global, as well as for the NH and SH (left to right), difference (dAOD₅₅₀) between syAOD and aAOD for aAOD binned in 0.2 intervals: median bias (circles) and bias standard deviation (error bars) for all and background (aAOD \leq 0.2) AOD types (purple), aerosol fine-dominated AOD (blue) and coarse-dominated AOD (green). The fraction (F) of points in each bin from the

total number of matchups is represented by orange bars. The fraction of fine-dominated matchups in each bin is shown as the blue dashed-line.

6.1.2 Monthly and seasonal results

380 Monthly (Jan, Feb, Mar, etc.), seasonal (DJF, MAM, JJA, SON) and annual (Year) variation of the validation results for S3A and S3B $syAOD_{550}$ for the globe, NH and SH are shown in Figure 5.

Correlation coefficient R is of sinusoidal shape for monthly statistics with two maxima for both S3A and S3B in the NH. In the SH, correlation coefficient varies strongly along the year. A clear peak (0.8-0.9) for both S3A and S3B is observed in Jun-Oct. Rms in the NH is within 0.25-0.32 for both S3A and S3B, with minimum in Oct-Jan and maximum in Mar-May. In the SH, rms for S3B is 0.15-0.2 in Dec-May and 0.09-0.14 in the other months.

385 Bias varies from 0.06 to 0.14 in monthly statistics in the NH. In the SH, bias is lower; it varies from 0.01 to 0.08 in monthly statistics. For S3B, bias is 0.01-0.35 lower than for S3A in all months, except April.

The fraction of matchups in the EE reflects well the difference between the NH and SH and between S3A and S3B. EE is, in general, higher for S3B with the offset up to 15% in the NH.

390 As a short summary, $syAOD_{550}$ validation results are slightly better for S3B; retrieval algorithm produces better results in the SH. Obtained validation results confirm that back scatter contribution to the radiance measured at the top of the atmosphere is less critical in the SH.

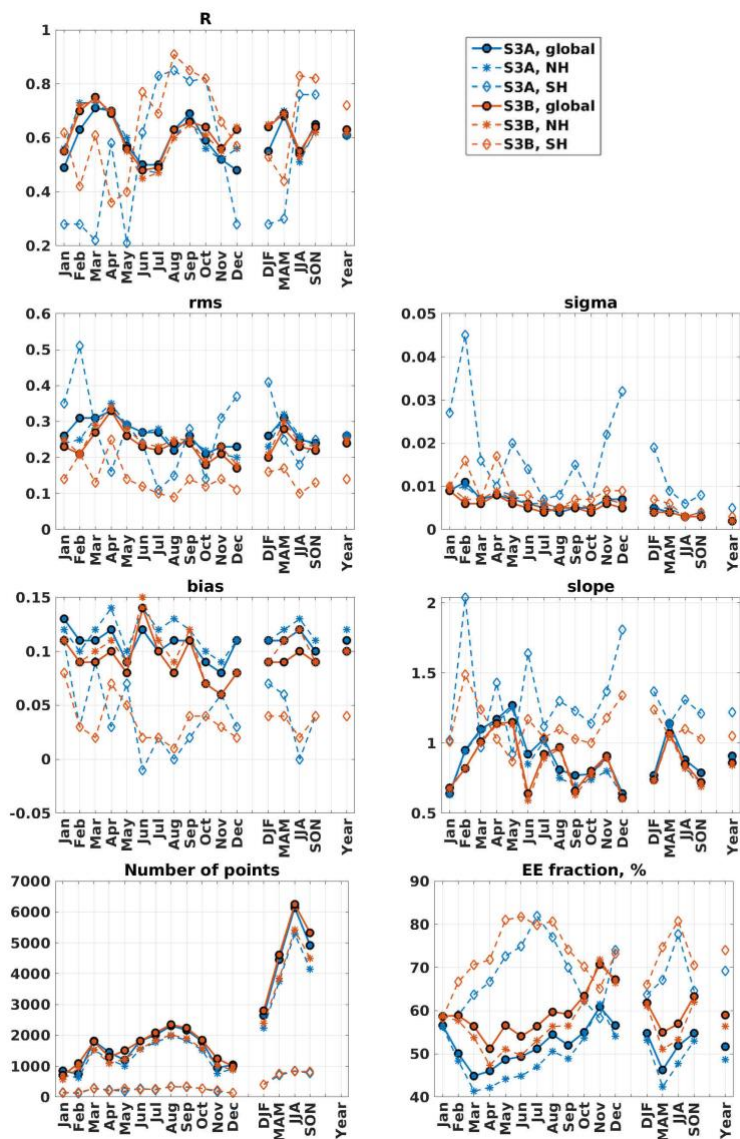


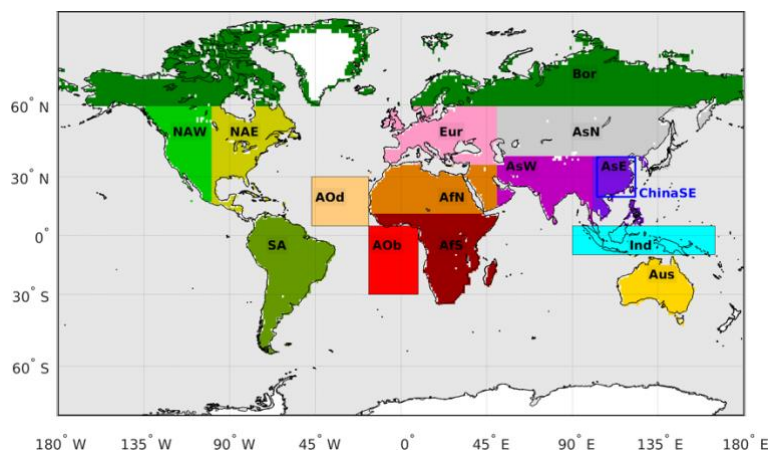
Figure 5: Validation statistics for syAOD₅₅₀ aggregated monthly (Jan, Feb, ..., Dec), seasonally (DJF, MAM, JJA, SON) and yearly (Year) shown as time series for S3A and S3B for the globe, NH and SH.

395 6.1.3 Regional performance

There are noticeable regional differences in the performance of the retrieval algorithm, which depend on, e.g., AOD load and AOD types (composition and optical properties), as well as on the properties of underlying surfaces. Retrieval quality (accuracy, precision and coverage) varies considerably as a function of these conditions, as well as whether a retrieval is performed over land or over ocean.

400 Following Sogacheva et al. (2020), we inter-compare validation results over 15 regions (as defined in **Error! Reference source not found.**) that seem likely to represent a sufficient variety of aerosol and surface conditions. These are shown in and

include 11 land regions, two ocean regions and one heavily mixed region. The land regions represent Europe (denoted by Eur), Boreal (Bor), northern, eastern, and western Asia (AsN, AsE and AsW, respectively), Australia (Aus), northern and southern Africa (AfN and AfS), South America (AmS), and eastern and western Northern America (NAE and NAW). South-Eastern China (ChinaSE), with is part of the AsE, is considered separately. The Atlantic Ocean is represented as two ocean regions, one characterised by Saharan dust outflow over the central Atlantic (AOd) and a second that includes burning outflow over the southern Atlantic (AOB). The mixed region over Indonesia (Ind) includes both land and ocean. For exact locations, see Table S2 in the Supplement.



410

Figure 6: Land and ocean regions defined for this study (as in Sogacheva et al., 2020): Europe (Eur), Boreal (Bor), northern Asia (AsN), eastern Asia (AsE), western Asia (AsW), Australia (Aus), northern Africa (AfN), southern Africa (AfS), South America (SA), eastern North America (NAE), western North America (NAW), Indonesia (Ind), Atlantic Ocean dust outbreak (AOd), Atlantic Ocean biomass burning outbreak (AOB). In addition, Southeast China (ChinaSE), which is part of the AsE region, marked with a blue frame, is considered separately. Land, ocean and global AOD were also considered.

415

High diversity in the validation results was observed between the selected regions (Figure 7; Table S2 in the Supplement). Highest correlation (0.94) was found in AOB region (the number of matchups is low (22) in this region). For ChinaSE, AsN, AsE, AOd, Aus, NAE, correlation coefficient R was in the range 0.6-0.8, which was higher than that for the globe. For Eur and Ind, $R < 0.4$. For above mentioned regions, bias between binned syAOD and aAOD does not change much. Bias is positive in Asia, Bor and SA regions for $aAOD < \sim 1.2$; bias calculated with linear regression was higher for those regions. The amount of syAOD outliers, defined as $|syAOD - aAOD| > 0.5$, varied among the regions. In Eur, positive syAOD outliers were observed for $aAOD < 0.3$. For Asian and Bor regions, syAOD outliers were observed mostly for aAOD in the range of [0.2, 1.2]. More negative syAOD outliers were observed in the NAW region.

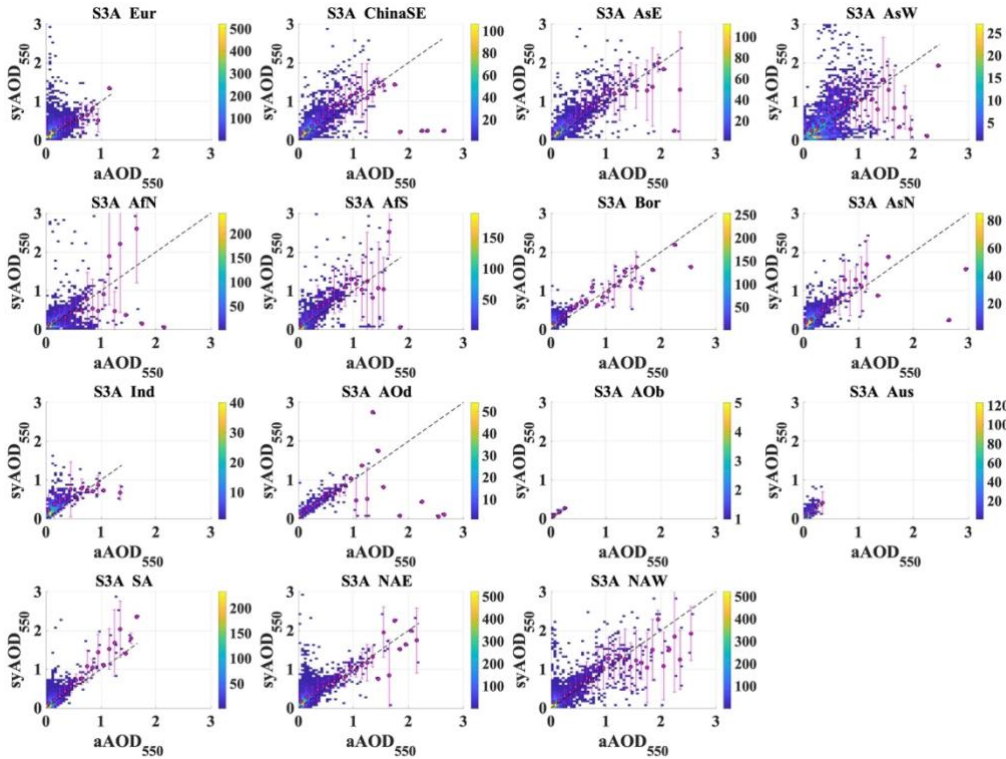
420

Among the land regions, the fraction of the pixels in EE was highest in Aus (81,6%), lowest in Bor and SA (<30%); for other land regions fraction of the pixels in EE was in the 30%-60% interval. Over ocean, in AOB and AOD areas, fraction of the pixels in EE was high (67,8% and 95,5%, respectively).

425

The fraction of syAOD pixels which satisfy GCOS requirements was low (<31%) for all regions, except for Aus (54,5%) and

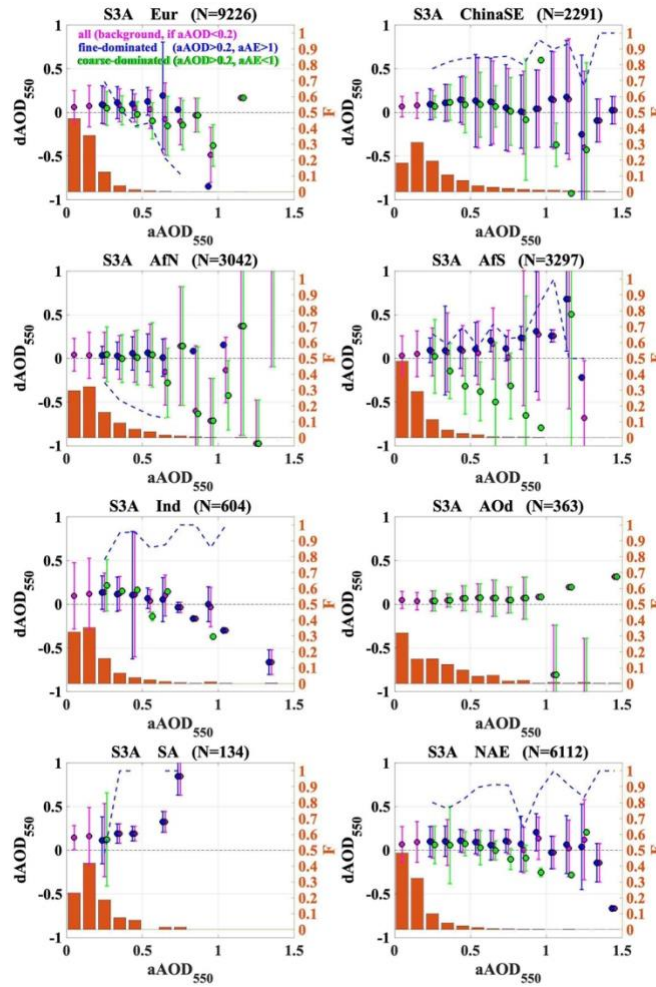
AOb (68,2%), where matchups cover low (<0.3) AOD conditions only.



430

Figure 7: For S3A, syAOD and aAOD scatter density plots for selected regions (as defined in Figure 6).

Regional differences between syAOD and aAOD for all aerosol types (including background (aAOD ≤ 0.2) AOD), fine-dominated and coarse-dominated AOD for selected aAOD bins are shown in Figure 8. For most of the regions, a general tendency towards positive SY_2 AOD offsets is observed under the background conditions. Offsets are higher (up to 0.15) in
 435 Ind and SA and lower (<0.04) in AfN, AfS and AOd. The behavior of the fine-dominated offset is similar for most of the regions (ChinaSE, AfN, AfS, Ind) with gradual increase in the aAOD range of ca 0.7-1.1. Coarse-dominated offset over Eur is underestimated by up to 0.18 for aAOD of 0.6-0.8. Over China, coarse-dominated offset is slightly overestimated at aAOD<0.7 and underestimated at aAOD>1. Over bright surface with contribution of dust aerosols (AfN), all groups show a good agreement with aAOD for aAOD<0.7. For aAOD>0.7, syAOD for coarse-contaminated matchups is considerably
 440 underestimated. Similar offsets are observed in NAE region, where 70-90% of matchups are characterized with fine-dominated aerosols. In possible biomass burning region (AfS), an underestimation of syAOD for coarse-dominated matchups gradually increases for aAOD>0.3 reaching -0.9 at aAOD close to 1. Over Ind, dAOD is positive for aAOD <0.5. Over ocean, with possible contamination of Saharan dust (AOd), offsets are constantly positive (up to 0.1) for all groups at aAOD<1.



445 **Figure 8:** Regional (for Eur, ChinaSE, AfN, AfS, Ind, AOd, SA, NAE) difference ($dAOD_{550}$) between syAOD and aAOD for aAOD binned in 0.1 intervals: median bias (circles) and bias standard deviation (error bars) for all and background ($aAOD \leq 0.2$) AOD types (purple), aerosol fine-dominated AOD (blue) and coarse-dominated AOD (green). The fraction (F) of points in each bin from the total number of matchups is represented by orange bars. The fraction of fine-dominated matchups in each bin is shown as blue dashed-line. Results for other regions are in the Supplement (Figure S 7)

450 6.1.4 Analysis of syAOD relative offsets

syAOD offset analysis was performed for matchups which did not satisfy the GCOS requirements of $|syAOD - aAOD| < 0.03$ or $|syAOD - aAOD| < 0.1 \times aAOD$ (GCOS, 2016).

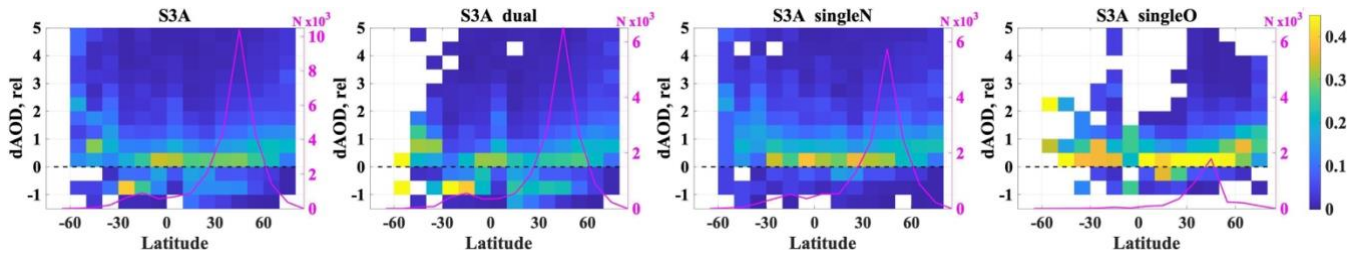
syAOD relative offset, or $dAOD_{rel}$, was defined as in eq.1:

$$dAOD_{rel} = \frac{syAOD - aAOD}{aAOD} \quad (\text{eq.1})$$

455 6.1.4.1 Latitude dependence of the syAOD relative offset

In Figure 9 we show a density scatter plot for the latitude dependence of the relative offset of the syAOD for all, dual, singleN and singleO groups of pixels for S3A. Colour indicates the fraction of the points with corresponding dAOD,rel from the total number of points within the 10° latitude bin. As an example, for the latitude in [20°S, 30°S], dAOD,rel was between -0.5 and -1 for ~38% of matchups. Magenta line shows the number of matchups in x-axis bin.

460 In the NH, dAODrel was mostly positive (syAOD was higher than aAOD). In the SH, dAOD,rel is mostly positive in 30°S-60°S and mostly negative in 10°S-30°S, except for the singleN group, where dAOD,rel is mostly positive. In both NH and SH, dAOD,rel is increasing towards the poles. This increase is more pronounced for the singleO group of pixels, but also visible in the dual group.



465

Figure 9: For S3A, density scatter plot for latitude (in degrees) dependence of the syAOD relative offset for ‘all’, ‘dual’ and ‘singleN’ groups of pixels (vertical panels from left to right, respectively). Colour indicates the fraction of the points with corresponding dAOD,rel interval from the total number of points within the latitude bin. Magenta line shows the total number of the matchups in the corresponding latitude bin.

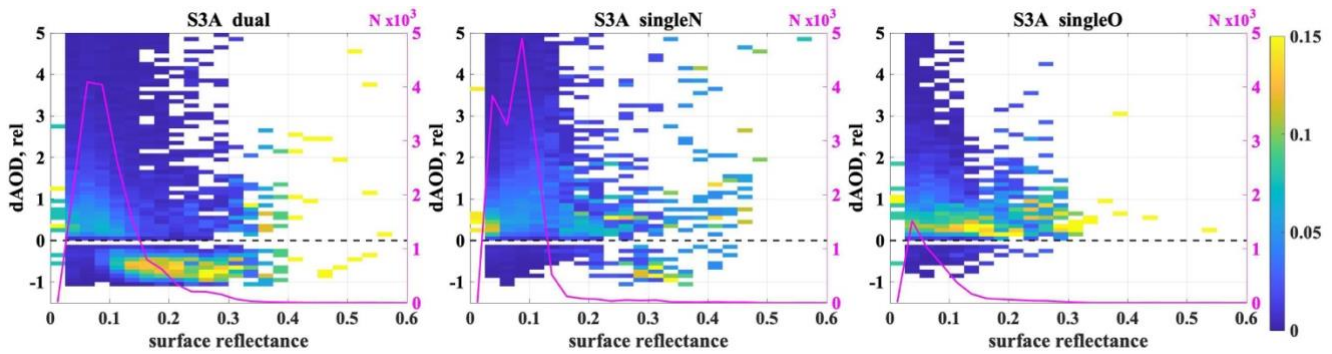
470 6.1.4.2 Dependence of syAOD relative offset on surface reflectance.

The directional surface reflectance (SR) retrieved with the SYNERGY algorithm is provided in the SY_2_AOD product.

In Figure 10 we show a density scatter plot for the dependence of the relative offset of the AOD on the retrieved SR for the dual, singleN and singleO groups of matchups. Colour indicates the fraction of the points with corresponding dAOD,rel from the total number of points within the surface reflectance bin.

475 For all matchups (not shown here), as well as for the dual group (globally, as well as over the NH and SH), footprints for the dAODrel dependence on the SR are similar. For SR < 0.05 and SR > 0.35, dAOD,rel indicates that syAOD is mostly overestimated. In specified ranges, dAOD,rel is increasing towards outer edges. For the SR in the range of 0.05-0.35, syAOD is mostly underestimated. Underestimation is more pronounced when syAOD is retrieved with the dual processor. For the singleO group, syAOD is mostly overestimated in all SR ranges.

480



485 **Figure 10:** For S3A, syAOD matchups with AERONET which do not satisfy GCOS requirements, scatter density plot for the dependence of the syAOD relative offset of retrieved surface reflectance for ‘all’, ‘dual’ and ‘singleN’ groups of pixels (vertical panels from left to right, respectively). Colour indicates the fraction of the points with corresponding dAOD,rel interval from the total number of points within the surface reflectance bin. Magenta line shows the total number of the matchups in the corresponding surface reflectance bin.

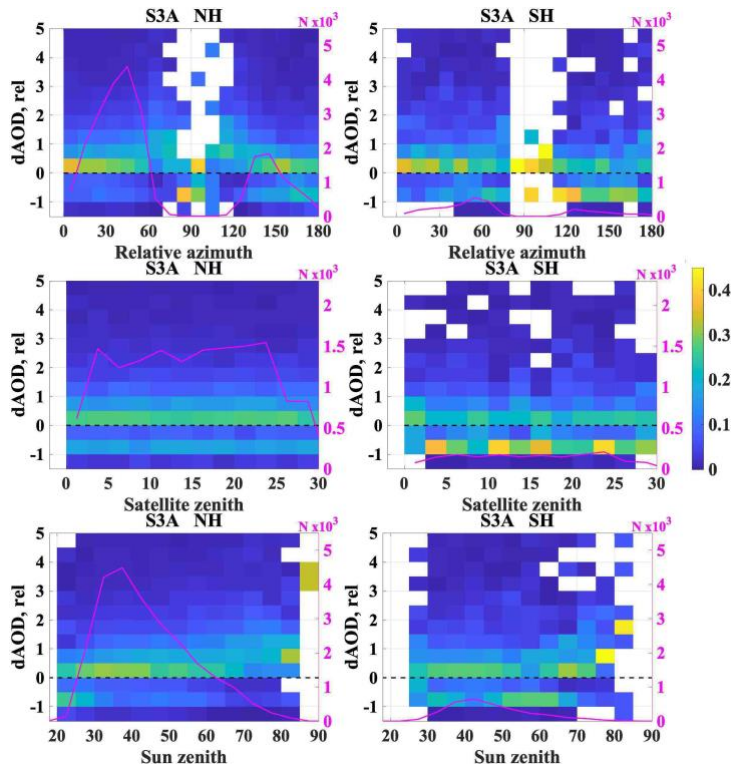
6.1.4.3 Dependence of the AOD relative offset on solar and satellite geometry

In Figure 11 we show the dependence of the syAOD relative offsets on the OLCI geometry (relative azimuth (Raz), satellite zenith angle (SatZA) and sun (or solar) zenith angle (SunZA) provided in the SY_2_AOD product, North and Heckel, 490 2019) for the NH and SH. Colour indicates the fraction of the points with corresponding dAOD,rel interval in the Raz, SatZA, or SunZA bins.

In the NH, positive dAOD,rel is increasing for Raz in [50°, 80°] and in [100°, 140°]. In the SH, we see the similar dependence of dAOD,rel for Raz in [50° 80°]. For Raz>90°, positive dAOD,rel is increasing with Raz increase from 150° to 180°; negative dAOD,rel of [-1, -0.5] is observed more often than positive [0 0.5] dAOD,rel.

495 No significant dependence of dAOD,rel on the SatZA was observed. However, a greater number of negative dAOD,rel is clearly seen in the SH.

In the NH, dAODrel is slightly positive (0-0.5), in all range of SunZA, except for the most extreme values. For SunZA>80°, the percentage of higher positive dAOD,rel (0.5-1) increases, while for SunZA<30° the percentage of higher negative dAOD,rel rises. In the SH, similar dependence was observed, except for SunZA in the range of 50°-65°, where dAOD,rel is 500 mainly negative.



505 **Figure 11:** For S3A, syAOD matchups with AERONET which do not satisfy GCOS requirements, the dependence of the AOD relative offsets on relative azimuth (upper panel), satellite zenith angle (middle panel) and sun zenith angle (lower panel) for the NH (left panel) and SH (right panel) for all pixels. Colour indicates the fraction of the points with corresponding dAOD,rel from the total number of points within the x-axis bin. Magenta line shows the total number of the matchups in the corresponding x-axis bin.

6.1.5 Linear regression considering provided syAOD uncertainties

Linear fitting for combinations of syAOD₅₅₀ and aAOD₅₅₀ collocations has been performed with a consideration of the syAOD₅₅₀ and aAOD₅₅₀ uncertainties (<https://se.mathworks.com/help/stats/linearmodel.predict.html>, last access 08 March 2022). For syAOD₅₅₀, pixel-level uncertainties are provided in the SY_2_AOD product. For aAOD₅₅₀, uncertainty of 0.01
 510 has been considered (Eck et al., 1999). For both S3A and S3B, for all groups of matchups, bias and slope for the linear regression fits applied to the whole AOD range were improved when the syAOD and aAOD uncertainties were considered. Bias was lowered roughly by 50%. Slope was improved by 10-15%. Improvements were smaller for singleO group of matchups (retrievals over ocean), for which the syAOD uncertainties are smallest (Sect. 6.2).

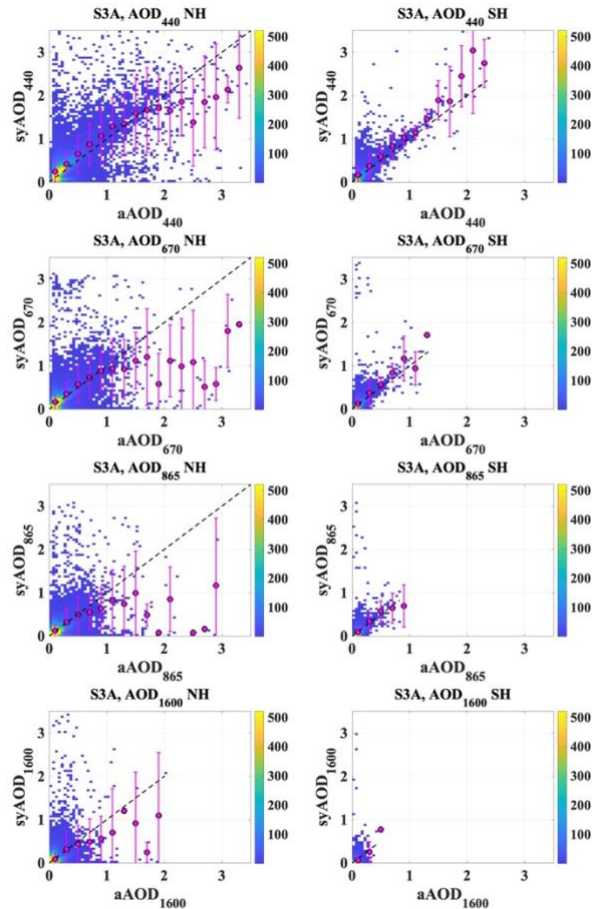
For more details, see Fig. S7 and Table S3, both in the Supplement.

515

6.1.6 AOD at other than 550nm wavelengths

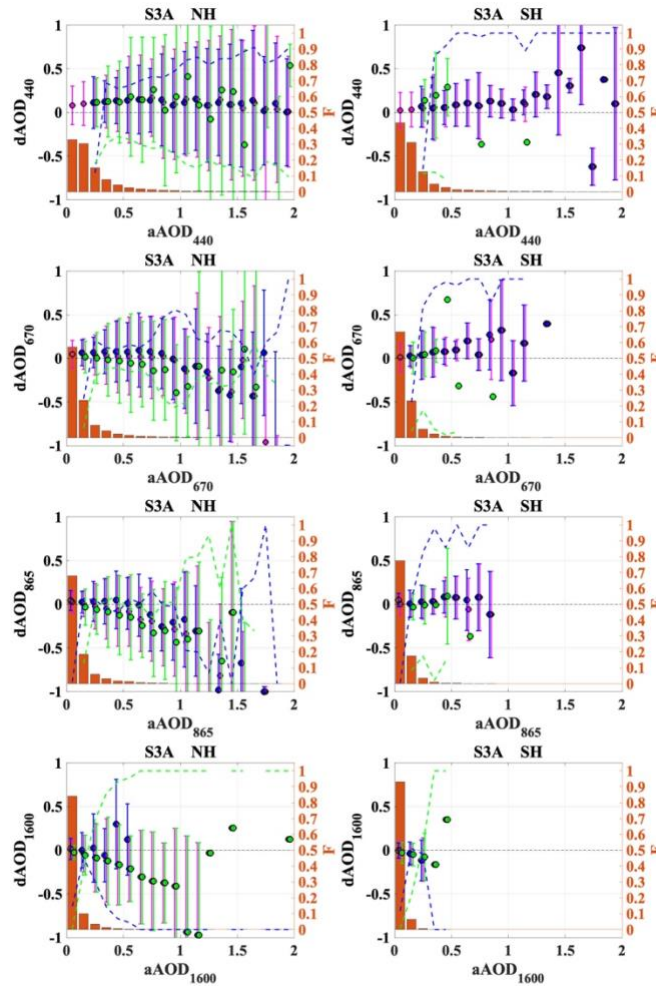
Scatter plots for SY_2 AOD₄₄₀, AOD₆₇₀, AOD₈₆₅, and AOD₁₆₀₀ are shown in Figure 12. Clear tendencies in validation statistics were observed when comparing validation results from shorter (440 nm) to longer (1600 nm) wavelengths. Though the correlation coefficient is decreasing (0.65/0.55/0.50/0.40 for 440/670/865/1600 nm respectively), the offset (0.15/0.1/0.07/0.05) and rms (0.33/0.23/0.18/0.16) are also decreasing. Note, that AOD is decreasing significantly (except for dust aerosols) as wavelength increases.

Validation statistics for all wavelengths are slightly worse for the NH than global validation statistics (Table S4, Supplement); validation statistics for the SH are considerably better than for the NH (except for R for 1600nm wavelength).



525 **Figure 12: Scatter plots for SY_2 AOD₄₄₀, AOD₆₇₀, AOD₈₇₀, and AOD₁₆₀₀ (panels top down) for the NH and SH (left and right panels, respectively).**

syAOD₄₄₀ is overestimated for all aerosol types (Figure 13). syAOD₆₇₀ for fine-dominated matchups is in a good agreement with aAOD₆₇₀ for aAOD₆₇₀<1. Similar tendency, though for narrower aAOD ranges (aAOD₈₇₀<0.5 and aAOD₁₆₀₀<0.3), is observed for syAOD₈₆₅ and syAOD₁₆₀₀. For all wave lengths, coarse-dominated syAOD is retrieved accurately for aAOD below ca. 0.4; above 0.4 syAOD is underestimated and offset between syAOD and aAOD is increasing with increasing aAOD.



535 **Figure 13:** for the NH (left) and SH (right), for different wavelengths (top down: 440, 670, 865, 1600 nm), the difference ($dAOD_{550}$) between syAOD and aAOD for selected aAOD bins: median bias (circles) and bias standard deviation (error bars) for all (incl. background, $aAOD_{550} \leq 0.2$) AOD types (purple), aerosol fine-dominated AOD (blue) and coarse-dominated (green) AOD. The fraction (F) of fine-dominated matchups from the total number of matchups in each bin is represented by orange bars. The fraction of fine- and coarse-dominated matchups in each bin is shown as blue and green dashed-lines, respectively.

6.2 AOD uncertainties

540 The concept for validation of the AOD uncertainties applied in the current study follows the validation strategy suggested by Sayer et al. (2013, 2020) with consideration of the validation practice further developed in the ESA Aerosol_cci+ project (Product Validation and Intercomparison Report, https://climate.esa.int/media/documents/Aerosol_cci_PVIR_v1.2_final.pdf, last access: 25 February 2022).

Definitions for uncertainties in the current evaluation of uncertainties are as following:

- 545 - Prognostic (per-retrieval) uncertainties (PU) for SY_2_AOD product are provided at 440, 550, 670, 865, 1600 and 2250 nm wavelengths.
- Expected discrepancy (ED) is an uncertainty variable which accounts for the PU and the accuracy of the ground-based (AERONET) data (AU), as defined by Sayer et al. (2020) in eq.2:

$$ED = \sqrt{PU^2 + AU^2} \text{ (eq.2)}$$

550 According to Giles et al. (2019), AU = 0.01.

- AOD error (AODerror) is a difference between satellite product AOD (syAOD) and AERONET AOD (aAOD); AOD absolute error (absAODerror) is an absolute value for AODerror.

Mean-bias correction has been performed for the error distributions in some of the subsequent analysis, since the concept of standard uncertainties requires bias-free error distributions which can be interpreted as absence of remaining systematic and quantifiable biases (https://climate.esa.int/media/documents/Aerosol_cci_PVIR_v1.2_final.pdf, last access: 25 February 2022).

If wavelength is not specifically mentioned, all variables in Section 6.2 are referring to the wavelength of 550 nm.

Analysis of the distribution of the uncertainties has been performed for the whole S3A and S3B SY_2_AOD product, as well as for groups of pixels retrieved with different retrieval approaches (dual, singleN, singleO). Results for S3A and S3B are similar; only results for S3A are shown and discussed.

6.2.1 χ^2 test for evaluation of the prognostic uncertainties

The goodness of the predicted uncertainties was estimated with the χ^2 test, as in eq.3

$$\chi^2 = \frac{1}{N-1} \sum_{i=1}^N \bar{\delta}_i \text{ (eq.3),}$$

where individual weighted deviation $\bar{\delta}_i$ is described in eq.3.

$$565 \quad \bar{\delta}_i = \frac{(syAOD_i - aAOD_i - \text{mean}(syAOD - aAOD))^2}{PU_i^2 + AU^2} \text{ (eq.4)}$$

If $\chi^2 \sim 1$, prognostic uncertainties describe well the AODerror. If $\chi^2 \gg 1$, PU are strongly underestimated; if $\chi^2 \ll 1$, PU are strongly overestimated. χ^2 was calculated for the whole dataset and for different AOD bins to reveal if the goodness of the PU uncertainties is AOD dependent.

For the whole dataset, $\chi^2 = 3.1$, which means that PU are slightly underestimated. For the binned AOD, χ^2 is varying strongly (Figure 14). For aAOD < 0.4, which is ca 90 % of all values, χ^2 fits into the interval [1.8 3.2]. Thus, for most of the matchups, PU is only slightly underestimated. For AOD > 0.4 PU underestimation is more pronounced.

No significant dependence of $\bar{\delta}_i$ on AODerror or surface reflectance provided in the SY_2_AOD product has been revealed (Figure S 6, Supplement).

Though the number of the matchups in the whole dataset is high (which provides the confidence to χ^2 test results), it was noticed that high $\bar{\delta}_i$ (up to 155) exists, which may bias the evaluation of the PU with χ^2 . To remove possible contribution of

the outliers on the χ^2 test results, cases with $\bar{\delta}_i > 10$ (which are less than 5 % of the total number of matchups) were removed from the analysis.

For the dataset with the removed outliers, $\chi^2 = 1.2$, which means that PU describe well the AODerror.

Influence of $\bar{\delta}_i$ outliers is more pronounced for AOD bins, where the number of matchups per bin is lower and thus the contribution of the outliers to the results is more expected. If $\bar{\delta}_i$ outliers are removed from the binned analysis, χ^2 fits to the range [1 1.45] for AOD < 0.4 (Figure 14).

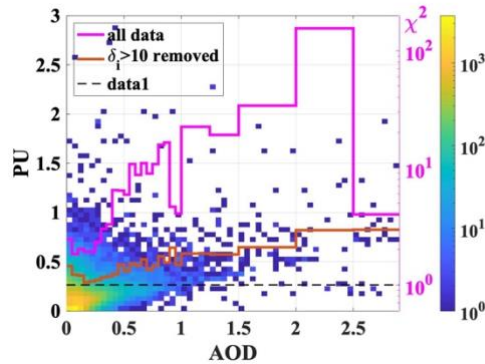


Figure 14: χ^2 for binned aAOD for all available matchups (magenta line) and after the outliers of the individual weighted deviations ($\bar{\delta}_i > 10$) are removed (red line). Density scatter plot for PU and syAOD.

6.2.2 Evaluation of prognostic uncertainties with absolute AOD error

To qualitatively illustrate an accuracy of prognostic uncertainties, we show in Figure 15 the comparison between the PU, AOD error distribution, and theoretical Gaussian distribution (with a mean of 0 and standard deviation of the syAODerror). PU distribution shows a double peak, (first peak is at ca. 0.02-0.04 for all groups; the second peak in a range of 0.12-0.18, for different groups). For singleN, two peaks are located close to each other. Mean PU for dual group is higher; std is higher for singleN group. AOD error distributions are Gauss-like with partly some asymmetry in positive AODerror direction.

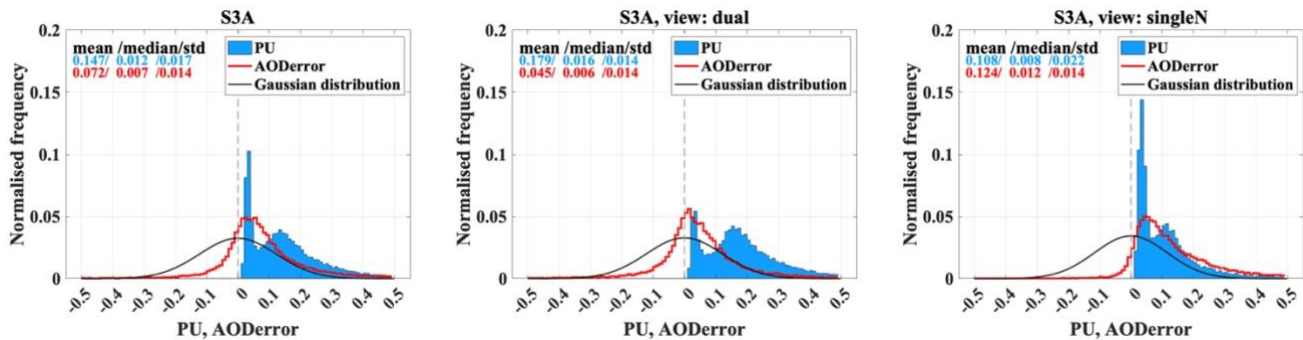


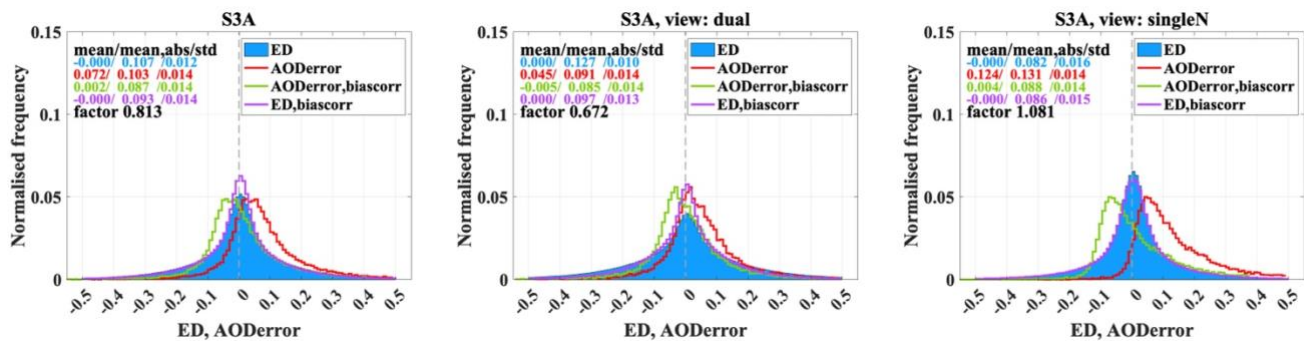
Figure 15: Comparison between PU, AOD error distribution and theoretical Gaussian distribution for the whole product (left panel), dual- (middle panel) and singleN (right panel) groups of matchups.

595 6.2.3 Evaluation of expected discrepancy and absolute AOD error

ED is calculated for each pixel by combining PU and AERONET uncertainties, as in eq.2.

For a quantitative validation, we follow (with some modifications) a new approach developed by ESA Aerosol CCI (https://climate.esa.int/media/documents/Aerosol_cci_PVIR_v1.2_final.pdf, last access: 25 February 2022). A synthetic cumulative distribution of ED is calculated assuming a Gaussian error distribution (normalized to a total integral of 1) with standard deviation of ED. In the next step, this synthetic error frequency distribution is compared with the AODerror. We calculate and subtract the mean bias from the AODerror distribution to make it more symmetric for direct comparison to the synthetic distribution (which by its definition is always symmetric). Bias correction results for S3A all, dual and singleN (0.07, 0.04 and 0.12, respectively) are shown in Figure 16. Figure 16.

Finally, we calculate an average correction factor for the synthetic distribution (and thus the prognostic uncertainties) in relation to the mean-bias corrected error distributions as the ratio of the absolute means of both distributions. Corrections factors are different for all matchups, dual and singleN groups. A small correction is needed for all and singleN (0.80 and 1.1, respectively). For the dual group, the correction is stronger (0.67); ED should be lowered.



610 **Figure 16: Histograms of the ED (blue filled bars), AODerrors (red; with bias correction: green) and ED calculated from uncertainties (purple; scaled to best fit the mean-bias corrected error distribution) for all matchups (left panel), dual- (middle panel) and singleN (right panel) groups of matchups. Statistics, mean/mean,abs/std are mean over ‘real’ values, mean over ‘absolute’ values and standard deviation, respectively, for histograms of the corresponding color.**

615 However, the correction method applied here is not equally improving ED in all ranges. The correction factor is biased by the number of pixels with small (<0.2) absAODerror. Thus, for those cases the correction works well; overestimated ED is lowered by 0.8/0.65 for all and dual groups. For absAODerror > ca.0.3, where ED is underestimated, correction degrades ED and increases disagreement between ED and AODerror. Possible solution can be in performing correction separately for different absAODerror ranges but setting specific relations for different groups between ED and absAODerror makes the analysis very complicated.

620

6.2.4 Potential of the expected discrepancy

Sayer et al. (2020) suggested the analysis of the potential of the PU to discriminate between ('good' and 'bad') pixels with likely small / large errors. Instead of PU, we perform analysis of the ED, which, besides PU, includes uncertainties of the ground-based measurements.

625 To estimate the potential of ED, we plot the absolute errors below which 38% of all pixels are, as a function of binned ED (Figure 17Figure 17). We then repeat this for the fractions 68% and 95%. These percentages relate to 0.5σ , 1σ , and 2σ (where σ is a standard width) for normal error distributions in each bin (along the vertical axis). Theoretically expected values are shown as dashed lines in black, red, and blue. The number of pixels per ED bin is shown as a grey dashed line.

The percentile plots show a reasonable agreement (within statistical noise) with the theoretical lines of 38% and 68% for majority of the validation points in the lower range of ED (up to 0.05-0.2) for all groups, with underestimation of the true error at higher values of ED for 38% and 68% lines. For the dual view case, ED overestimates the true error, while for the single view case the true error is higher than the ED prediction, especially at higher values of ED ($ED \gg 0.2$).

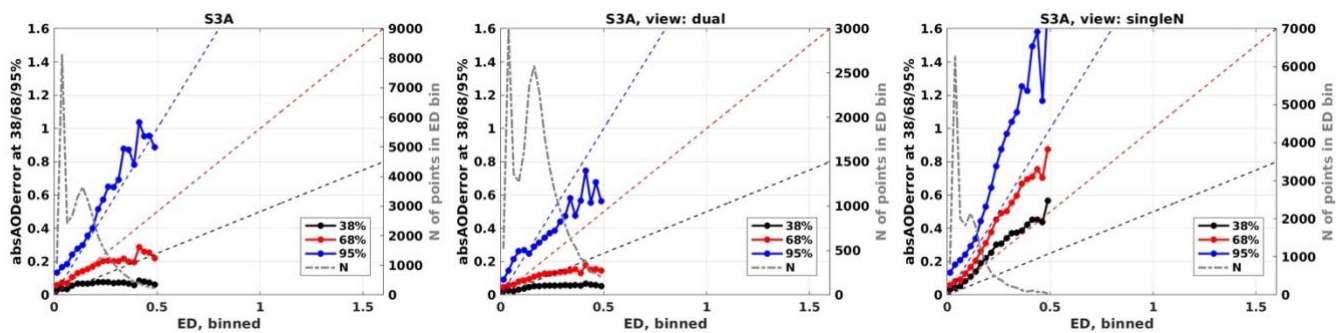
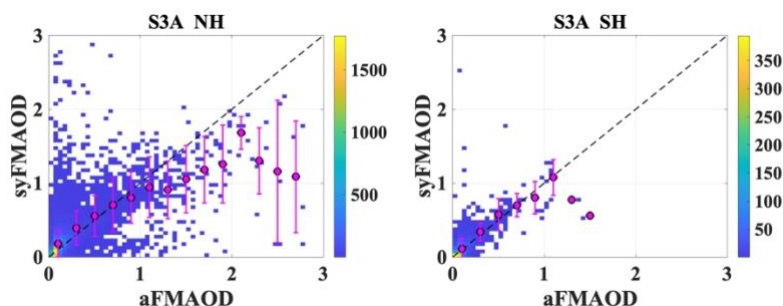


Figure 17: Percentile plots of absAODerrors at 38% (black), 68% (red) and 95% (blue) as function of binned expected discrepancy.

635 6.3 Fine mode AOD and Fine Mode Fraction

Fine mode AOD in the SY_2 product (syFMAOD) is provided at 550nm, while AERONET Fine mode AOD (aFMAOD) is provided at 500 nm. As for aAOD₅₀₀ (Sect. 6.1), AOD spectral dependence (https://aeronet.gsfc.nasa.gov/new_web/man_data.html, O'Neill et al., 2003, last access: 25 February 2022) and AERONET AE exponent were considered to convert aFMAOD₅₀₀ into aFMAOD₅₅₀.

640 Density scatter plots for the relation between syFMAOD and aFMAOD in the NH and SH, are shown in Figure 18Figure 18 for S3A; validation statistics are summarised in Table 2 for both S3A and S3B. The dispersion of points is higher in the NH. Validation results are considerably better in the SH: R is higher (0.67 vs 0.63 for the SH and NH, respectively), rms (0.15 vs 0.23) and bias (0.06 vs 0.14) are lower, slope (0.93 vs 0.70) is closer to 1. Analysis of the binned FMAOD shows that in both NH and SH, good agreement was observed between syFMAOD and aFMAOD for aFMAOD < 1. At aFMAOD > 1, syFMAOD is considerably underestimated in the NH. In the SH, only few aFMAOD values above 1 are measured. Validation statistics for S3B are slightly better.



650 **Figure 18: Density scatter plots for S3A syFMAOD and corresponding aFMAOD for collocations available over the NH (left) and SH (right).**

Looking at the seasonal validation results, for both S3A and S3B, the correlation coefficient is slightly higher in MAM (0.65 /0.67, for S3A/S3B, respectively) and JJA (0.67/0.69) and lower (0.56/0.59) in DJF (Table 2; Figure S9, Supplement). Bias is ca 0.1-0.12 and slightly higher (0.15/0.12) in JJA. The binned mean syFMAOD values are close to the 1:1 line for aFMAOD < 0.6-1 but fall below the line for higher aFMAOD.

655

Table 2: For S3A and S3B, annual (for the globe, NH and SH) and seasonal (for the globe) validation statistics for syFMAOD.

Period	Region	N		R		rms		std		bias		slope	
		S3A	S3B	S3A	S3B	S3A	S3B	S3A	S3B	S3A	S3B	S3A	S3B
year	globe	18145	18262	0.63	0.67	0.22	0.20	0.001	0.001	0.13	0.12	0.72	0.72
	NH	15883	15982	0.63	0.66	0.23	0.20	0.002	0.001	0.14	0.12	0.70	0.71
	SH	2262	2280	0.67	0.72	0.15	0.15	0.003	0.002	0.06	0.06	0.93	0.91
DJF	globe	2447	2418	0.56	0.58	0.21	0.18	0.004	0.003	0.12	0.10	0.59	0.53
MAM		5832	5952	0.65	0.67	0.22	0.21	0.002	0.002	0.12	0.11	0.85	0.86
JJA		7641	7579	0.67	0.69	0.23	0.20	0.002	0.002	0.1	0.13	0.71	0.70
SON		2225	2313	0.49	0.66	0.22	0.16	0.004	0.003	0.12	0.10	0.56	0.62

660 Among selected regions, offset for all aerosol types is negligible (slightly positive) in Eur, Ind and NAW (Figure 19). In ChinaSE and AfN, an offset is increasing with increasing of aFMAOD over 0.5 and becomes more unstable (takes both positive and negative values).

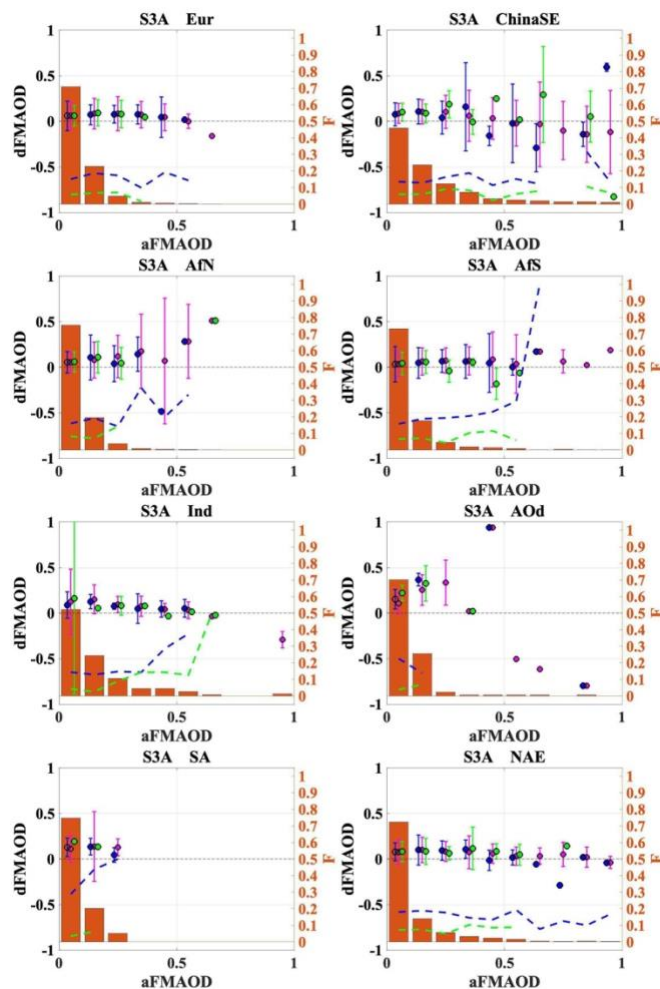


Figure 19: Regional (for Eur, ChinaSE, AfN, AfS, Ind, AOd, SA, NAE) difference (dFMAOD) between syFMAOD and aFMAOD for selected aFMAOD bins: median bias (circles) and bias standard deviation (error bars) for all AOD types (purple), aerosol fine-dominated AOD (blue) and coarse-dominated AOD (green). The fraction (F) of points in each bin from the total number of matchups is represented by orange bars. The fraction of fine-dominated matchups in each bin is shown as orange dashed-line. Results for other regions are in the Supplement (Figure S 10).

SY_2 Fine Mode Fraction (syFMF), which is a fraction of syFMAOD from the total syAOD, was validated against AERONET Fine Mode Fraction (aFMF). Since syFMAOD is slightly overestimated, we expect that syFMF is overestimated as well. Density scatter plots for the relation between syFMF and aFMF in the NH and SH are shown in Figure 20 for S3A. In both hemispheres, and thus globally, syFMF is overestimated in the aFMF range of 0-0.7; positive offset of 0.3-0.5 at low (<0.25) aFMF is gradually decreasing. At aFMF>0.9, syFMF is slightly underestimated. Offset between syFMF and aFMF is slightly lower in the SH. For the NH/SH respectively, R is 0.34/0.42; bias is 0.56/0.49, slope is 0.28/0.37.

675

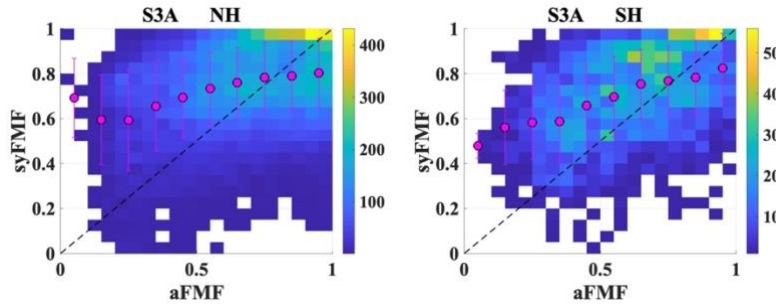


Figure 20: Density scatter plots for S3A syFMF and corresponding aFM for collocations available over the NH (left) and SH (right).

Scatter density plot between dFMF (which is defined as a difference between syFMF and aFMF) and aAOD is shown in Figure 21 for the NH and SH. In general, offset is higher at low AOD and decreases towards high AOD. The fraction of high (>0.05) overestimates is decreasing towards high AOD, while the fraction of high underestimates increases.

680

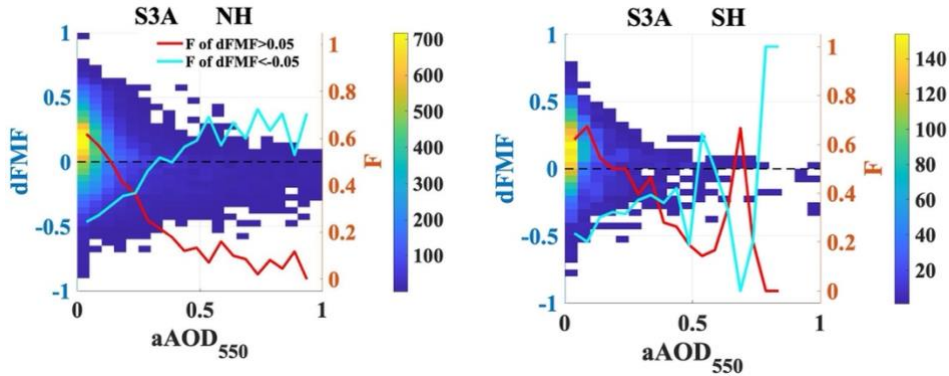
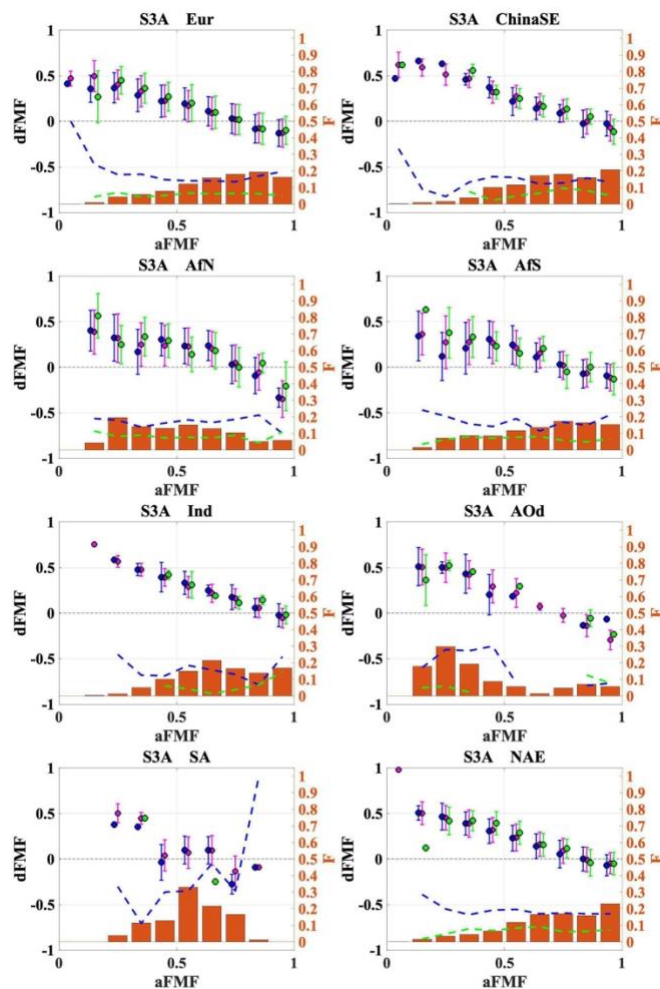


Figure 21: Density scatter plot for the difference (dFMF) between syFMF and aFMF as a function of aAOD₅₅₀. Fractions of positive (dFMF>0.05, red line) and negative (dFMF<-0.05, blue line) overestimations per aAOD bin are shown.

Regional dFMF (Figure 22) is positive (0.3-0.7) for low (<0.2) aFMF and decreasing gradually towards higher aFMF. At aFMF above 0.5-0.7, aFMF turns to negative (syFMF is underestimated). Similar tendency is observed for all chosen regions.



685

Figure 22: Regional (for Eur, ChinaSE, AfN, AfS, Ind, AOd, SA, NAE) difference (dFMF) between syFMF and aFMF for selected aFMF bins: median bias (circles) and bias standard deviation (error bars) for all AOD types (purple), aerosol fine-dominated AOD (blue) and coarse-dominated AOD (green). The fraction (F) of points in each bin from the total number of matchups is represented by orange bars. The fraction of fine-dominated matchups in each bin is shown as orange dashed-line. Results for other regions are in the Supplement (Figure S 11).

690

6.4 Ångström exponent

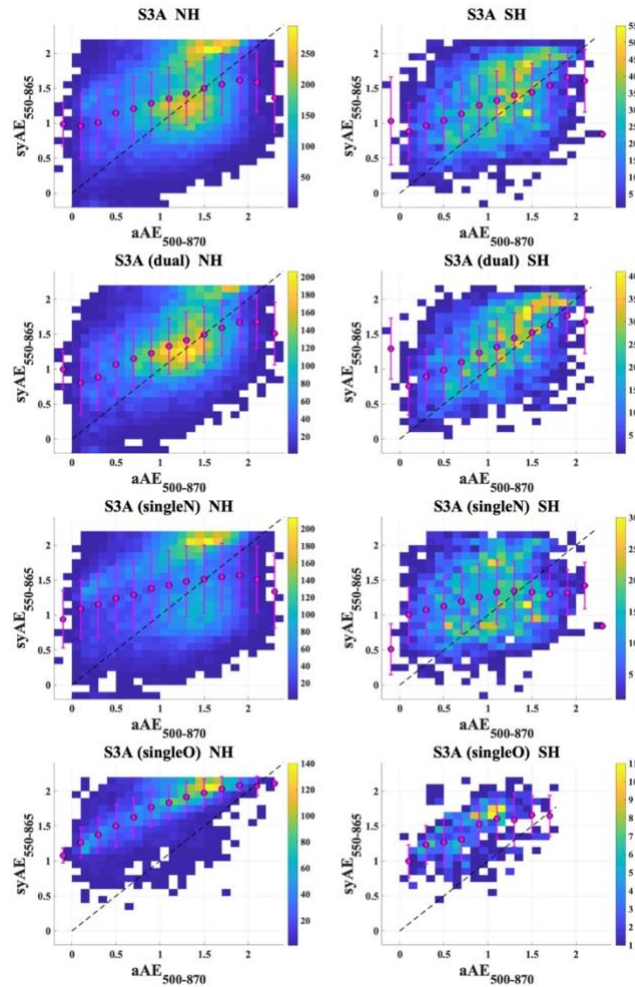
The Ångström exponent, AE, is often used as a qualitative indicator of aerosol particle size. Synergy AE (syAE) is calculated in the spectral interval 550-865 nm, while AERONET AE (aAE) is provided for 500-870 nm. The difference between $AE_{550-865}$ and $AE_{500-870}$ depends on the aerosol type and may be as high as 5-10% of AE (personal estimations). This difference must be considered for the interpretation of the evaluation results.

695

Scatter plots between $syAE_{550-865}$ and $aAE_{500-870}$ for S3A for all matchups and different groups of matchups are shown in Figure 23, corresponding validation statistics are shown in Table S5, Supplement. Two “clouds” of satellite/AERONET AE matchups are clearly observed. The first cloud is in the aAE interval of [1, 1.6] and syAE around 1.2. In that interval, the cloud of pixels

is located around the 1:1 line, which means that the agreement between syAE and aAE is quite good. Dual matchups contribute most to this “cloud”. The second “cloud”, formed mostly from the singleN and singleO groups of matchups, is in the aAE interval of [1.4, 1.9] and syAE around 2. In that interval, syAE is overestimated by 0.3-0.6.

For 40% of the matchups with AERONET in the NH, and for 60% of the matchups in the SH, which fit into the aAE interval of [1, 1.8], an offset between syAE and aAE is within ± 0.25 . General overestimation of low (< 0.5) syAE and underestimation of high (> 1.8) syAE is resulting in high (0.94, globally) overall bias.



705

Figure 23: Scatter plots between syAE₅₅₀₋₈₆₅ and aAE₅₀₀₋₈₇₀ for S3A for the NH and SH (panels left and right, respectively) for different groups of products (top-down: all, dual, singleN and singleO).

For the whole global product, correlation coefficients between syAE₅₅₀₋₈₆₅ and aAE₅₀₀₋₈₇₀ are quite low, 0.35/0.34, rms is high, 0.57/0.58 for S3A/S3B, respectively. Validation statistics are slightly better for the dual product. The singleO product shows

710 better correlation, but worse rms and std. Validation statistics are better in the NH for all matchups and the dual product. For
 for the single view groups (singleN and singleO), no difference in validation results was revealed between the NH and SH.
 Regional analysis (Figure 24, Table S6) reveals considerable differences in syAE evaluation results for regions with different
 surface type and aerosol properties. Footprints for the frequency of matchups at certain AE ranges (density value on the scatter
 plot) follow the “cloudy” shape in regional scatter density plots. Location of the “clouds” along x-axis (aAE) is specified by
 715 prevailing aerosol types in those regions. The “cloudy” shape of the footprint often ruins validation statistics, which should be
 interpreted with consideration of the matchup’s footprint, Figure 24.

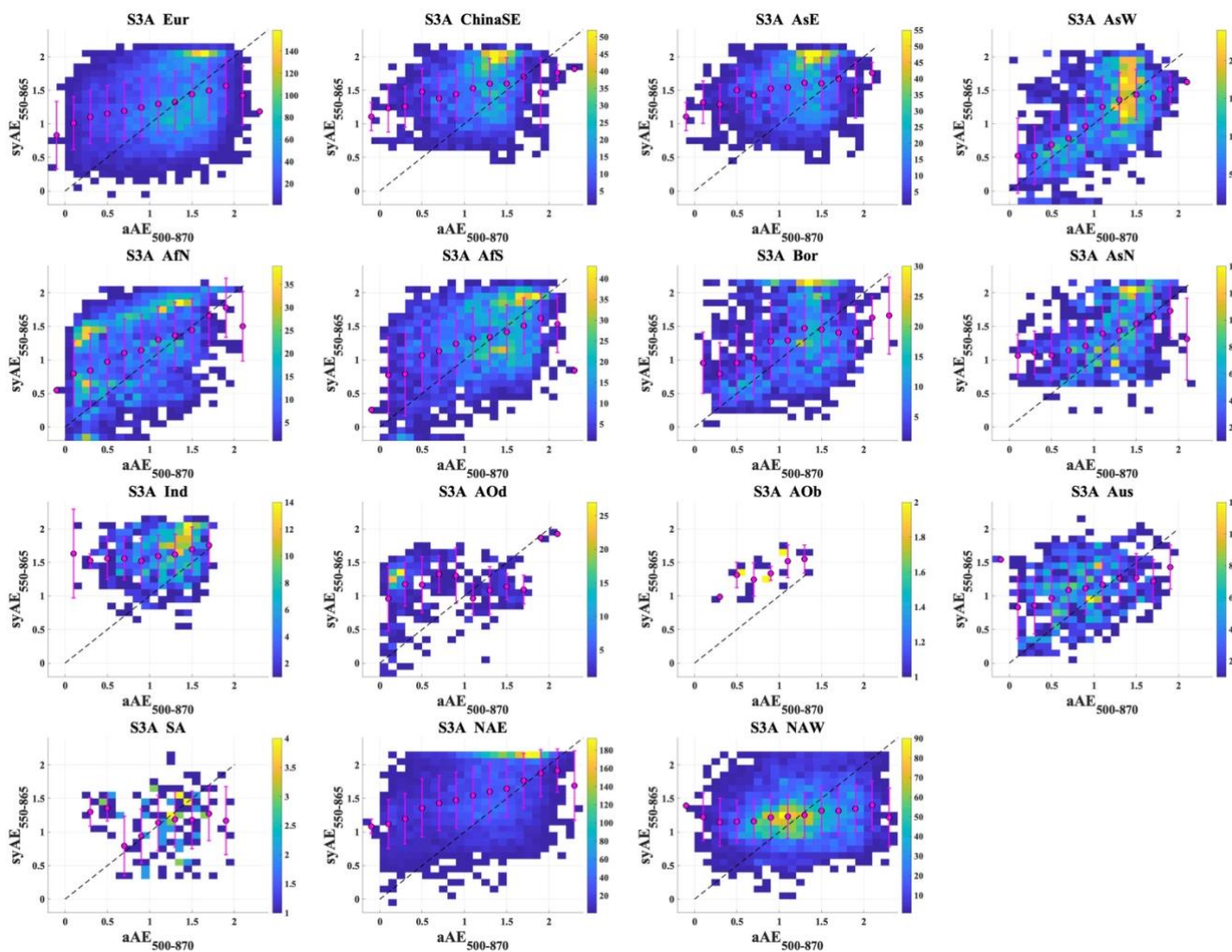


Figure 24: Regional scatter density plots between $syAE_{550-865}$ and $aAE_{500-870}$. Regions are defined in Figure 6.

720 $syAE$ is often overestimated in the aAE range [1.3, 1.7], except for AsW, where the fraction of “good” (close to the 1:1 line)
 pixels is as high as fraction of overestimated $syAOD$. In AfN, low AE, which is typical for that region characterized by a high

fraction of dust particles, is often highly overestimated. Dense cloud of “good” matchups is located near the 1:1 line in NAW. However, R (Table S6 in the Supplement) is low in that region, because, as mentioned above, the shape of the “good” pixels has a shape of a cloud and statistics are defined by outliers which are distributed evenly in all directions from the “cloud”. In oceanic regions with possible transport of dust aerosols, syAE is often underestimated. The low number of matchups in AOb region (N = 22) doesn’t allow making a solid conclusion on the syAE quality in this region.

7 Validation over ocean

Being performed on-board ships, MAN AOD measurements are irregular. S3A and S3B collocations with MAN for the period 01.2020-09.2021 are shown in Figure 25. Altogether, 105 matchups have been found for S3A and 95 matchups for S3B. Note, that about half of the collocations are observed near coastal zones. Since the number of validation points is low, we show in Figure 26 scatter plots and validation statistics for both S3A and S3B.

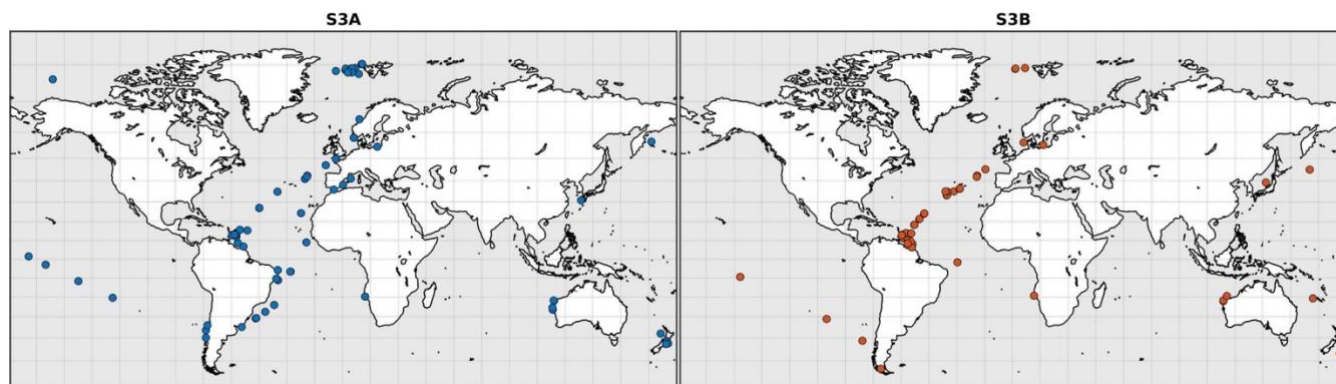


Figure 25: Collocations of S3A (left) and S3B (right) with MAN, 01.2020-09.2021

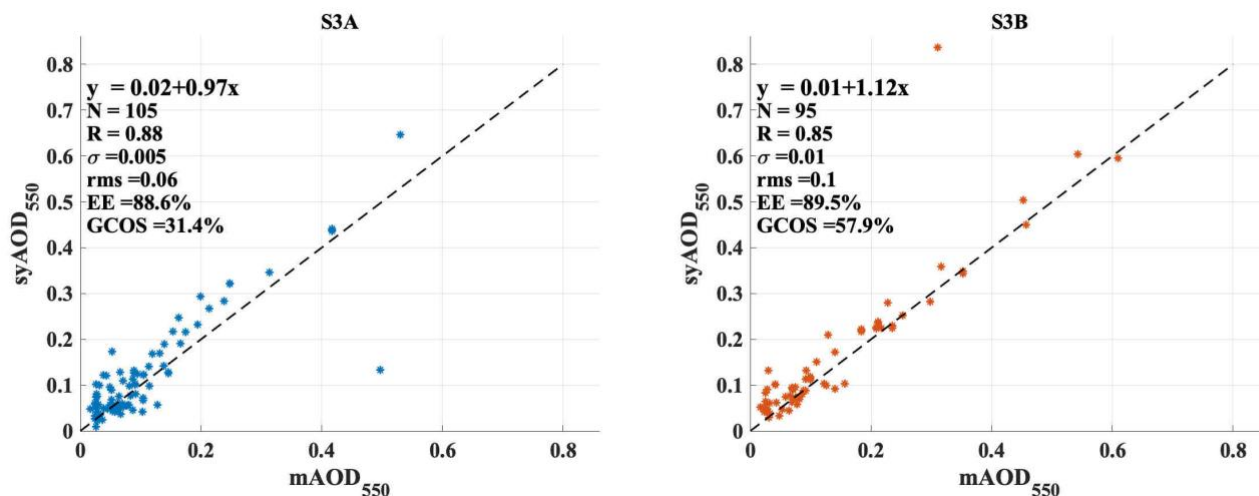


Figure 26: Scatter plots between S3A and S3B syAOD and MAN AOD (mAOD) with validation statistics.

Results for both instruments confirm a good performance of the retrieval algorithm over ocean. For S3A/S3B, correlation coefficients are 0.88/0.85, fractions of pixels in the EE are 88.6/89.5 %. An offset with MAN AOD (mAOD) is slightly higher for S3A (0.02/0.01), while rms is slightly higher for S3B (0.06/0.1).

740 One value from each product, S3A and S3B, can be considered as a clear outlier: S3A over the Baltic is underestimated, S3B over the Caribbean Sea is overestimated. The removal of these outliers from the validation exercise improves validation statistics: correlation increases to 0.95/0.97, rms decreases to 0.04/0.03, fractions of pixels in the EE increases to 89.4/92.4 % for S3A/S3B, respectively.

8 SY_2 AOD spatial performance relative to MODIS Terra DT&DB AOD product

8.1 Methods

745 The coverage of ground-based reference data is limited. To better evaluate a spatial distribution of the satellite retrieved AOD, the inter-comparison with other satellite products is necessary. The satellite product chosen as a “reference” must fulfil several criteria, e.g.:

- (i) overpass time as close as possible to Sentinel-3 to avoid possible different aerosol and cloud conditions;
- (ii) wider swath (for the reference product), which allows considering most of the pixels from the tested product in the analysis;
- 750 (iii) similar resolution, which allows pixel-to-pixel intercomparison.

Considering these criteria, the MODIS Terra DT&DB AOD product has been chosen as a reference for evaluation of the SY_2 AOD₅₅₀ product.

MODIS Terra DT&DB AOD product fulfils two out of three criteria mentioned above:

- (i) The Sentinel-3 orbit is a near-polar sun-synchronous orbit with a descending node equatorial crossing at 10:00 am Mean 755 Local Solar time. The MODIS Terra satellite is crossing the equator on descending passes at 10:30 -10:45 AM.
- (ii) SLSTR dual view swath centred on the sub-satellite track is 740 km wide, with a single view swath width of 1470 km. OLCI instrument covers a swath width of 1,270 km. MODIS Terra has a viewing swath width of 2,330 km.

The (iii) criteria is not fulfilled since MODIS and SY AOD products are provided at different resolutions. The resolution of the SY_2 product is 4.5x4.5 km², while the MODIS AOD daily product is available at 3km, 10km and 1° resolution, MODIS 760 monthly product is available at 1° resolution. Thus, to fulfil the third criterion, we re-grided daily SY_2_AOD product to 1° resolution for an area of interest (AOI) and calculated monthly aggregates. One degree grid resolution was chosen to mitigate collocation uncertainties, smooth the data and minimise the processing time.

Two different approaches exist for evaluation and inter-comparison of satellite monthly AOD. For algorithm performance inter-comparison, only the spatio-temporally collocated pixels from the two products were considered (used in monthly 765 aggregates). For climate studies (for, e.g., model evaluation, trend analysis), where existing monthly products are utilized, an inter-comparison should be performed for the products built on all points available for each instrument, respectively.

SY_2 and MODIS Terra AOD products were inter-compared over the area shown in Figure 27 and Figure 28. To evaluate and inter-compare AOD products (and thus algorithm performance) in different environments (e.g., surface type, aerosol type, aerosol loading), sub-regions shown in Figure 29 (top right) were chosen (see Table S7 for details).

770 **8.2 Inter-comparison of daily AOD products**

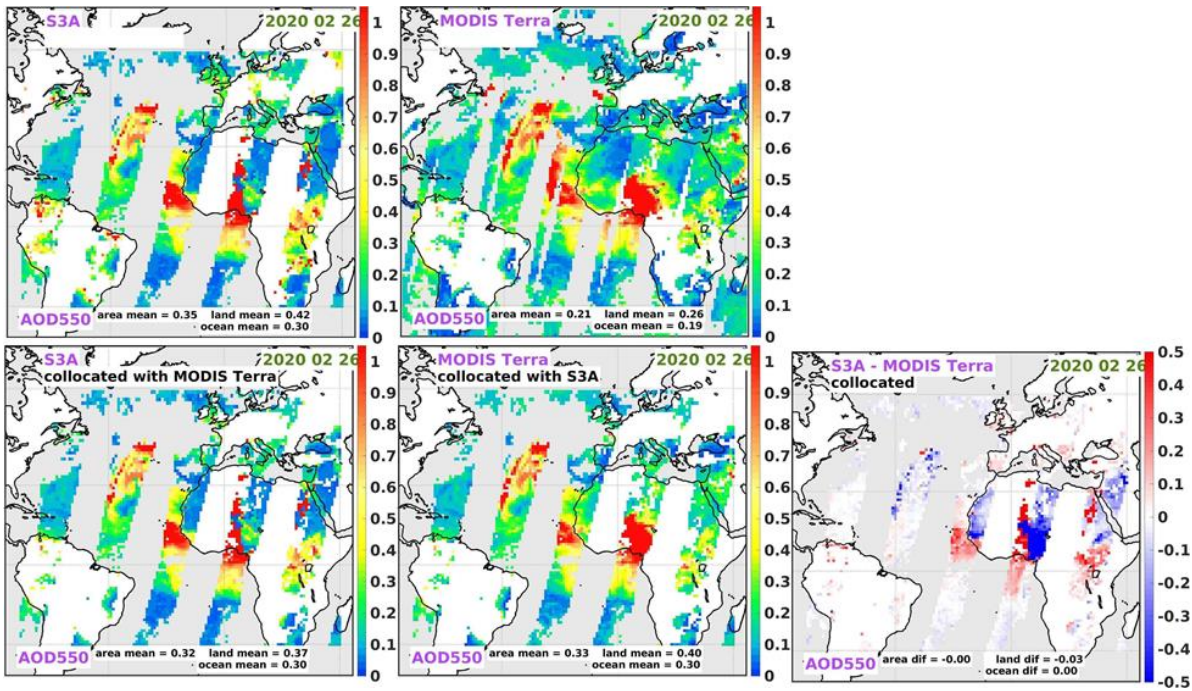
All pixels available in S3A SY_2_AOD and MODIS Terra L3 daily AOD550 products, collocated products and differences between collocated products are shown for a selected area of interest (AOI) for 26 February 2020 (Figure 27). Because of the wider swath, MODIS has larger coverage than S3A. Thus, when collocating two products for closer intercomparison, more pixels from the MODIS product are removed.

775 For the products containing all original pixels for each instrument respectively, the SY_2 AOD mean over the AOI is higher than MODIS Terra AOD (0.35/0.21 for S3A/ MODIS, respectively). Mean AOD over land and over ocean are also higher for S3A. For collocated products, mean (over the AOI) AOD for S3A and MODIS, as well as AOD over ocean come very close to each other. However, SY_2 FMF (syFMF) over ocean (Figure 28) is lower than MODIS FMF (modFMF). Also, regional differences related mainly to possible dust overflow over Atlantic, exists. MODIS provides higher AOD over the dust plume.

780 Lower modAOD on the west of the plume may be explained by the offset between MODIS Terra and S3A overpass time. Over land, mean AOD is slightly lower for S3A for collocated pixels. modFMF over bright surface (Sahara) is missing; over other regions the difference between syFMF and modFMF is lower compared to ocean.

For the chosen day, for S3A, a sharp transition between AOD retrieved over land and ocean at the west coast of Africa is revealed. This feature is clearly seen in the S3A and MODIS AOD difference plot. This can be explained by the land/surface gradient in the syFMF (Figure 28). The large AOD gradient in S3A data is observed over Nigeria; the inconsistency with MODIS data reaches above ± 0.5 AOD in this area. MODIS FMF is not provided in this area.

785



790 **Figure 27:** For 26 February 2020, upper panel: All pixels available in S3A syAOD₅₅₀ (left), MODIS modAOD₅₅₀ (middle) products. Lower panel: Pixels existing in both products (collocated products), syAOD₅₅₀ (left), modAOD₅₅₀ (middle) and difference between syAOD₅₅₀ and modAOD₅₅₀ (right). For each sub-plot, statistics (mean AOD for the whole area and separately for land and ocean) are shown.

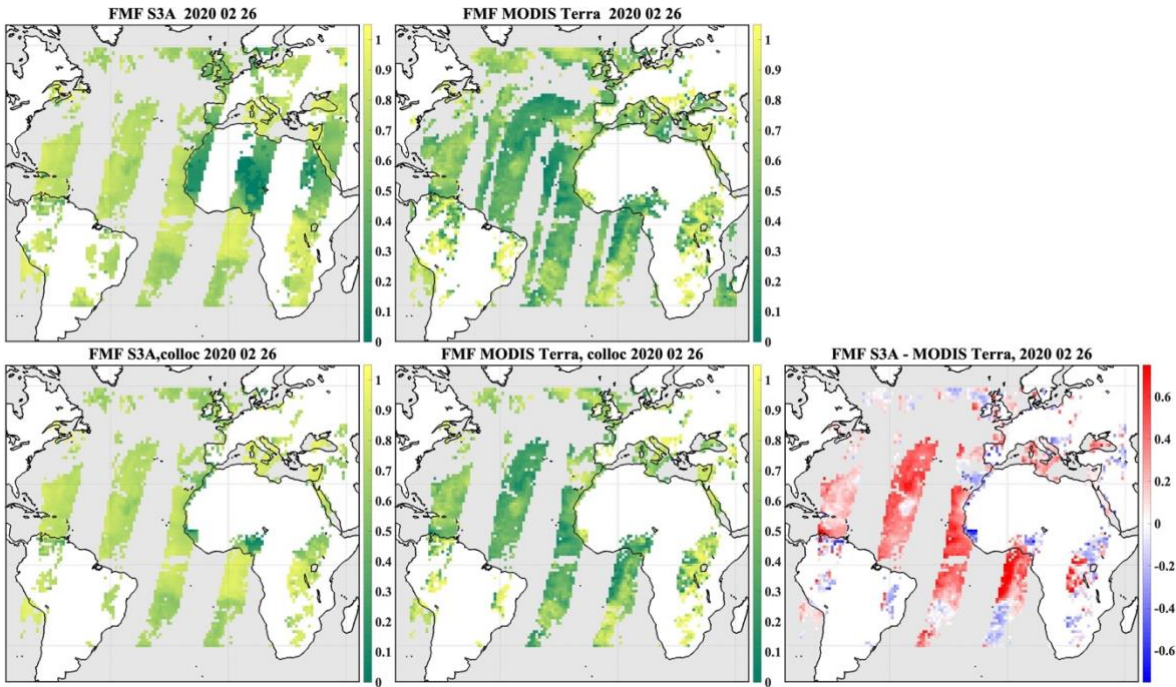


Figure 28: Same as Figure 27, syFMF, modFMF and difference between syFMF and modFMF

795 For the whole year 2020, S3A SY₂ and MODIS AOD₅₅₀ pixel-level inter-comparisons of 1°x 1° daily products for chosen sub-regions are shown as density scatter plots in Figure 29.

In Europe region, which includes parts of Eastern and Southern Europe and Middle East, AOD is low (<0.4) in both products, in general. However, several outliers are observed in SY₂ product (SY₂ AOD is in the range 1-4, while MODIS AOD is below 0.5). A possible reason for disagreement can be that SY₂ AOD was retrieved in cloud edge, while MODIS has been
800 retrieving AOD in clear sky condition (given ca 30 min difference between overpasses). If this is true, SY₂ cloud screening should be improved to better distinguish between aerosol and clouds in cloud edge areas. The outlier cases should be studied separately to better understand a reason for disagreement.

In the desert area the disagreement between the two products is most significant. For MODIS AOD in the range 0-0.8 most of the SY₂ pixels have AOD<0.2, while there are also a considerable number of SY₂ pixels with AOD in the range 1-4. For
805 MODIS AOD above 0.8, SY₂ AOD is often low, which is confirmed with averaged over MODIS AOD bins results (magenta dots in Figure 29). The high surface reflectance typical to this area is challenging for aerosol retrieval. The large variance observed in the AOD comparison indicates that a more detailed inter-comparison including the surface reflectance values retrieved by each algorithm should be performed. Over clean ocean and ocean+dust sub-regions, an agreement between SY₂ and MODIS AOD is quite good for modAOD<1 and modAOD<1.8, respectively; for higher AOD , syAOD is lower than
810 MODIS AOD.

In coast+dust area (over which biomass burning aerosols can be transported occasionally), AOD averaged over bins are biased slightly positive for AOD<1.2, which results from SY₂ positive outliers, while for AOD>1.2 SY₂ AOD is often much lower than MODIS AOD, thus binned averaged AOD is biased negative.

The footprints for SY₂ and MODIS AOD look similar in the two areas with seasonal contribution of biomass burning aerosols
815 (Africa,BB and S.America,BB). An agreement between SY₂ and MODIS is good for MODIS AOD below 1.2. Above that threshold, SY₂ AOD is on average lower.

Overall, the majority of data is in the low AOD range, where agreement is decent (with SY₂ slightly high biased), but at higher AOD there is much more variance (partly due to the scarcity of data), and in general a slight low-bias for SY₂.

Seasonal comparison is shown in Figure S13, supplement. Annual and seasonal statistics for SY₂ and MODIS Terra for all
820 daily pixel AOD inter-comparison are summarised in the supplement (Table S8).

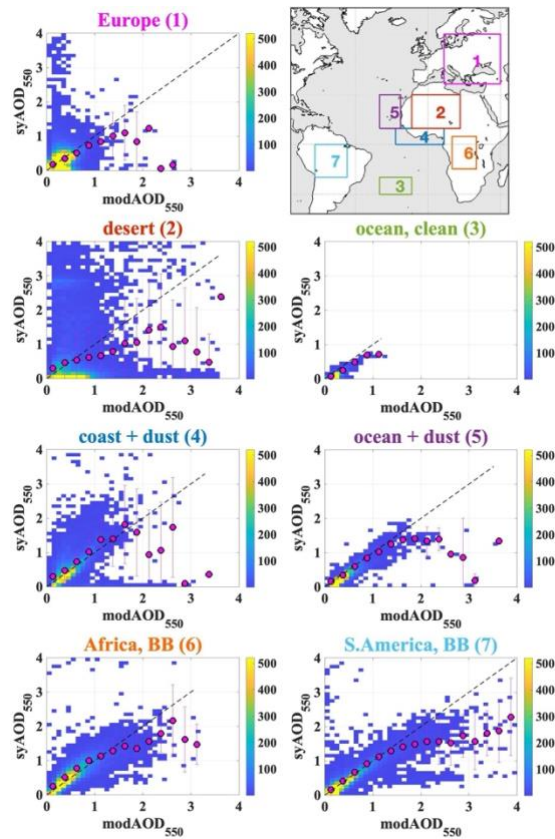


Figure 29: Density scatter plots for MODIS Terra and S3A SY_2_AOD L3 daily collocated products for 2020 for the sub-regions shown in the top right corner. Statistics are summarised in the Supplement (Table S9).

8.3 Spatial inter-comparison of seasonal and annual S3A and MODIS Terra AOD products

825 Two types of monthly datasets have been created from SY_2_AOD and MODIS Terra daily data to study the differences at monthly/seasonal/annual (MSA) level.

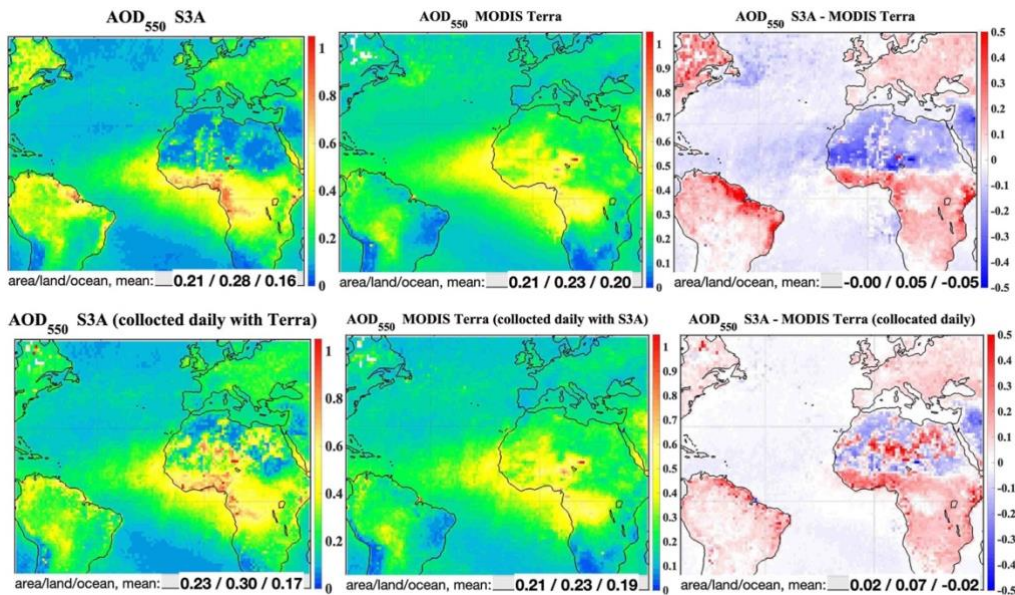
In the first monthly dataset, all pixels available in SY_2_AOD and MODIS Terra daily products have been used to build a monthly aggregate, respectively for each instrument. Inter-comparison of these ‘all pixels’ monthly aggregates (which are similar to the official monthly products provided for users) is important because it will help in, e.g., understanding the
 830 difference in climate data records which are built from the provided monthly AOD products which include all available data. A second monthly dataset, ‘collocated’ product, has been aggregated using only collocated daily pixels. Inter-comparison of ‘collocated’ monthly aggregates shows the difference in monthly AOD based on differences in retrieval approaches.

Annual AOD from ‘all pixels’ and ‘collocated’ monthly datasets for SY_2_AOD and MODIS Terra, respectively, and the corresponding differences are shown in Figure 30. Seasonal plots for collocated aggregates and difference between them are
 835 shown in Figure 31. Statistics for difference plots (area/land/ocean means) have been calculated from pixel-to-pixel difference, but not as difference between the AOD averaged over AOI, land and ocean.

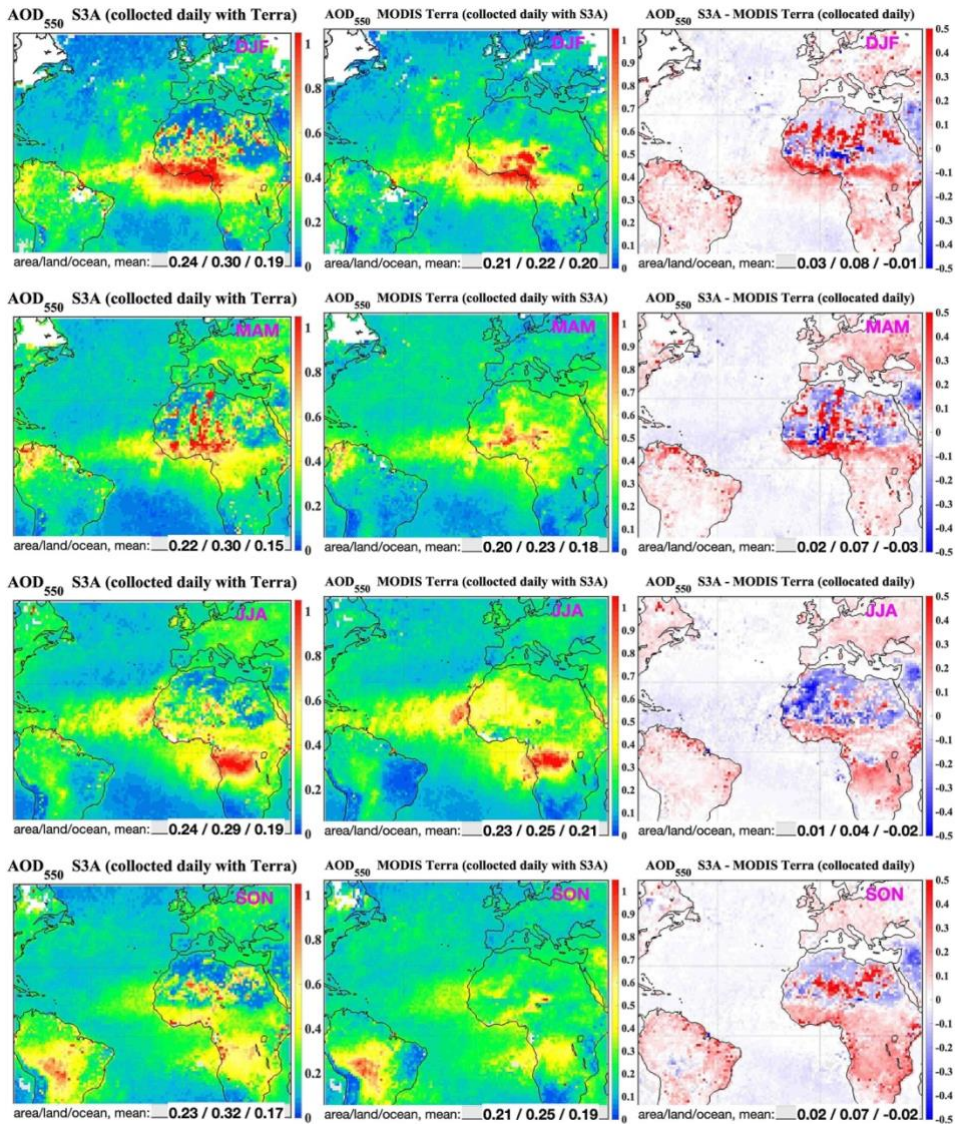
Differences between SY_2_AOD and MODIS Terra MSA AOD exist in both ‘all pixels’ and ‘collocated’ datasets. For both datasets, SY_2 AOD averaged over AOI is higher for the whole area, as well as for land and ocean. The difference is smoother for ‘all pixels’ datasets. Even though difference plots show that regional offset between two datasets is often within GCOS requirements of AOD quality (0.03) over ocean (SY_2 AOD is in general lower) and whole AOI, difference in AOD over land is often higher (up to 0.11 as averaged over AOI in DJF, ‘all pixels’ dataset).

Regional differences in seasonal AOD from the ‘collocated’ dataset are considerably higher (Figure 31). For all land sub-regions (except for ‘desert’, JJA), S3A AOD is higher than MODIS AOD. The offset is highest for ‘coast+dust’ region in DJF and for ‘Africa, BB’ region in SON (0.18 and 0.15, respectively). General tendency of decreasing offset towards JJA months has been observed. However, though the offset is often high, time series for both products are within an overlap (grey area) of the standard deviations for individual products. Highest negative offset (between 0.05 and 0.1) is observed in JJA in the ‘desert’ region. Regional differences in seasonal AOD from the ‘all pixels’ dataset are less scattered (Figure S6, Supplement).

For the open ocean regions (‘ocean, clean’ and ‘ocean+dust’), S3A AOD is in general lower than MODIS AOD for all MSA; the exceptions are January and February in ‘ocean+dust’ region (Figures not shown). In the annual scale, the offset between S3A and MODIS AOD is -0.02 for ‘ocean+dust’ and -0.03 for ‘ocean, clean’. AOD in ‘collocated’ dataset is higher compared to ‘all pixels’ dataset for both S3A SY_2 and MODIS Terra. Comparing with ‘all pixels’, ‘collocated’ SY_2 AOD product looks less smooth over Northern Africa in DJF and MAM.



855 **Figure 30:** For year 2020, annual S3A SY_2_AOD (left panel), MODIS Terra (middle panel) AOD and difference in between S3A and MODIS Terra (right panel) AOD. Annual means are calculated from monthly aggregates combined from all data available in each product (upper panel) and pixels of collocated daily AOD (lower panel). AOD mean and difference between SY_2 and MODIS AOD for the whole area, as well as separately for land and ocean, are shown on the maps.



860 **Figure 31: Seasonal (top down: DJF, MAM, JJA, SON) S3A (left panel), MODIS Terra (middle panel) AOD₅₅₀ and difference in AOD₅₅₀ between S3A and MODIS Terra (right panel). From monthly aggregates created from collocated daily S3A and MODIS Terra AOD products.**

9 Conclusions and recommendations for future evolution

We have presented the first validation of a new SYNERGY global aerosol product, derived from the data from the OLCI and
 865 SLSTR sensors onboard the Sentinel-3A and -3B satellites. Combined, the two satellites provide close to daily global coverage and provide aerosol measurements with a latency of 2-3 days. In this study we have compared the aerosol product with ground-based photometer data from four networks: AERONET, SKYNET, SURFRAD, and MAN, and with MODIS combined Dark

Target and Deep Blue algorithms. The aim of this study was to provide global characterisation of the current aerosol retrieval, and to guide future algorithm development.

870 Over ocean, the performance of SYNERGY retrieved AOD is good and consistent with reference MAN dataset (rms ~ 0.05), although the MAN validation has a limited set of higher AOD examples. Against MODIS, agreement is good, although SYNERGY AOD shows lower values at high AOD (>1.5) in dust regions, potentially indicating cloud screening improvement needed to correctly detect high dust levels.

Over land, overall performance has a much higher rms error, approximately 0.25 when compared to AERONET. Overall
875 AERONET correlation is ~ 0.6 . Reduced performance over land is expected since the surface reflectance and angular distribution of scattering are higher, and they are more difficult to treat over land than over ocean. However, the results show that these statistics are affected by a large number of outliers. Inspection of these outliers and patterns of disagreement with MODIS indicate possible reasons and targets for future algorithm evolution. The main causes are (i) poor screening of snow/ice covered surfaces, (ii) inadequate cloud screening in some regions. For example, in tropical forest areas, care needs to be taken
880 to fully exclude any pixels containing clouds, including sub-pixel clouds in either nadir or oblique view. In addition, removal of cloud edge pixels (cloud free pixels next to cloud masked pixels) should be considered. Bright desert surfaces also have less stable retrieval, with land/ocean contrast suggesting high values in dust plumes are underestimated over land. Further uncertainty is introduced by an error in a priori estimates of aerosol properties not retrieved, principally single scattering albedo (SSA).

885 It is clear that retrievals using dual view give higher quality, making use of more information to allow less reliance on surface spectral assumptions. Retrieval over land surface in the Northern Hemisphere shows generally higher retrieval error, including regions of boreal forest where we would expect higher quality retrieval due to the low surface signal. In some cases, this will be due to weak masking of snow and ice cover, and the presence of retrievals made at high solar zenith angles (over 70°) often excluded in other aerosol datasets. In addition, since the land retrieval relies on use of the oblique SLSTR view we expect to
890 see higher quality retrievals in the SH compared to NH. This is due mainly to sampling of backscattered light by the SLSTR oblique view in NH, where aerosol has a weak signal, and the surface signal is higher, while in SH the geometry is reversed. Over ocean this is not the case, as the retrieval is not reliant on the oblique view, and indeed the geometry results in less sunglint in NH ocean.

The retrieval of Angström exponent, related to aerosol size distribution, shows spatial correlation with expected sources but
895 generally overestimates AE for cases where AERONET Angström is low, resulting in overall high bias. This is dependent on the retrieval of fine mode fraction in the algorithm, which needs to be investigated further and improved. Evaluation of the per-retrieval uncertainty indicated good correlation with measured error distributions, with overprediction of expected error in dual view case, and underprediction in single view case. Evaluation of the uncertainty propagation is difficult in the presence of outliers which do not fit the algorithm assumptions, where we see a tail of higher errors, for example related to undetected
900 cloud in the input data.

Author contribution

CH, LS and SD created the original research framework and provided research direction. MD, CH established a data base. LS developed a validation strategy, wrote the software and performed the analysis. PK co-wrote the software. LS, TV, PN, 880 CH, SS and SD co-wrote the manuscript.

905 Competing interests

The contact author has declared that neither they nor their co-author has any competing interests.

Funding

This work has been performed in the frame of the LAW project under the European Space Agency Contract 4000129877/20/I-BG.

910 Data access

SY_2_AOD product: <https://scihub.copernicus.eu/dhus/#/home> , last access 13 March 2022

SY_2_AOD product validation matchups: <https://law.acri-st.fr/home>, last access 10 January 2022

References

- 915 Arbor, A., Briley, L., Dougherty, R., Wells, K., Hercula, T., Notaro, M., Rood, R., Andresen, J., Marsik, F., Prosperi, A., Jorns, J., Channell, K., Hutchinson, S., Kemp, C., and Gates, O.: A Practitioner’s Guide to Climate Model Scenarios. Great Lakes Integrated Sciences and Assessments (GLISA). https://glisa.umich.edu/wp-content/uploads/2021/03/A_Practitioners_Guide_to_Climate_Model_Scenarios.pdf, 2021.
- 920 Augustine, J. A., Hodges, G. B., Cornwall, C. R., Michalsky, J. J., and Medina, C. I.: An update on SURFRAD - The GCOS Surface Radiation budget network for the continental United States. *Atmos. and Oceanic Technol.*, 22(10), 1460-1472, doi:10.1175/JTECH1806.1., 2005.
- Bergquist, P., and Warshaw, C.: Does global warming increase public concern about climate change? *J. Polit.* 81, 686–691, 2019.
- Bevan, S.L., North, P.R.J., Los, S.O. and Grey, W.M.F.: A global dataset of atmospheric aerosol optical depth and surface reflectance from AATSR. *Remote Sensing of Environment*, 116, 119-210, 2012.
- 925 Borowitz, M.: Open space. The global effort for open access to environmental satellite data, Cambridge, MA, MIT Press, ISBN:9780262037181, 432 pp., 2018.
- Chu, D. A., Kaufman, Y. J., Ichoku, C., Remer, L. A., Tanre, D., and Holben, B. N.: Validation of MODIS aerosol optical depth retrieval over land. *Geophys. Res. Lett.*, 29, 8007, doi:10.1029/2001GL013205, 2002.
- 930 Committee on Earth Observation Satellites (CEOS); Coordination Group for Meteorological Satellites (CGMS). Space Agency Response to GCOS Implementation Plan–The Joint CEOS/CGMS Working Group on Climate (WGClimate). http://ceos.org/document_management/Working_Groups/WGClimate/Documents/Space%20Agency%20Response%20to%20GCOS%20IP%20v2.2.1.pdf, 2017.
- Cox, C. and Munk, W.: Measurements of the roughness of the sea surface from photographs of the Sun’s glitter. *J. Opt. Soc. Am.*, 44, 838–850, 1954.

- 935 Davies, W. & North, P.: Synergistic angular and spectral estimation of aerosol properties using CHRIS/PROBA-1 and simulated Sentinel-3 data. *Atm. Meas. Tech.*, 8(4), 1719-1731, 2015.
- de Leeuw, G., Holzer-Popp, T., Bevan, S., Davies, W., Descloitres, J., Grainger, R.G., Griesfeller, J., Heckel, A., Kinne, S., Klüser, L., Kolmonen, P., Litvinov, P., Martynenko, D., North, P. J. R., Ovigneur, B., Pascal, N., Poulsen, C., Ramon, D., Schulz, M., Siddans, R., Sogacheva, L., Tanré, D., Thomas, G. E., Virtanen, T. H., von Hoyningen Huene, W., Vountas, M., and Pinnock, S.: Evaluation of seven European aerosol optical depth retrieval algorithms for climate analysis. *Remote Sensing of Environment*, 162, 295-315. 10.1016/j.rse.2013.04.023, 2015.
- Dubovik, O., Schuster, G. L., Xu, F., Hu, Y., Bösch, H., Landgraf, J., and Li, Z.: Grand Challenges in Satellite Remote Sensing. *Front. Remote Sens.* 2:619818. doi: 10.3389/frsen.2021.619818, 2021.
- Eck, T. F., Holben, B. N., Reid, J. S., Dubovik, O., Smirnov, A., O'Neill, N. T., Slutsker, I., and Kinne, S.: Wavelength dependence of the optical depth of biomass burning, urban, and desert dust aerosols, *J. Geophys. Res.*, 104, 31,333–31,349, doi:10.1029/1999JD900923, 1999.
- ESA Aerosol CCI portal, available at: <https://climate.esa.int/en/projects/aerosol/key-documents/>, last access: 25 February 2022.
- Estelles, V., Campanelli, M., Utrillas, M. P., Exposito, F., and Martinez-Lozano, J. A.: Comparison of AERONET and SKYRAD4.2 inversion products retrieved from a Cimel CE318 sunphotometer. *Atmos. Meas. Tech.*, 5, 569-579, doi:10.5194/amt-5-569-2012, 2012.
- Eyre, J. R., Bell, W., Cotton, J., English, S. J., Forsythe, M., Healy, S. B., and Pavelin, E. G.: Assimilation of satellite data in numerical weather prediction. Part II: Recent years. *Quarterly Journal of the Royal Meteorological Society*, 1-36, <https://doi.org/10.1002/qj.4228>, 2022.
- 955 GCOS, 2016, https://ane4bf-datap1.s3.eu-west-1.amazonaws.com/wmod8_gcoss3fs-public/aerosols_ecv_factsheet_201905.pdf?Sv_8X3rsnl_rqNQVLEIg5gzig53zTHox, last access: 25 February 2022.
- Giles, D. M., Sinyuk, A., Sorokin, M. G., Schafer, J. S., Smirnov, A., Slutsker, I., Eck, T. F., Holben, B. N., Lewis, J. R., Campbell, J. R., Welton, E. J., Korkin, S. V., and Lyapustin, A. I.: Advancements in the Aerosol Robotic Network (AERONET) Version 3 database – automated near-real-time quality control algorithm with improved cloud screening for Sun photometer aerosol optical depth (AOD) measurements, *Atmos. Meas. Tech.*, 12, 169-209, <https://doi.org/10.5194/amt-12-169-2019>, 2019.
- 960 Gliß, J., Mortier, A., Schulz, M., Andrews, E., Balkanski, Y., Bauer, S. E., Benedictow, A. M. K., Bian, H., Checa-Garcia, R., Chin, M., Ginoux, P., Griesfeller, J. J., Heckel, A., Kipling, Z., Kirkevåg, A., Kokkola, H., Laj, P., Le Sager, P., Lund, M. T., Lund Myhre, C., Matsui, H., Myhre, G., Neubauer, D., van Noije, T., North, P., Olivié, D. J. L., Rémy, S., Sogacheva, L., Takemura, T., Tsigaridis, K., and Tsyro, S. G.: AeroCom phase III multi-model evaluation of the aerosol life cycle and optical properties using ground- and space-based remote sensing as well as surface in situ observations, *Atmos. Chem. Phys.*, 21, 87–128, <https://doi.org/10.5194/acp-21-87-2021>, 2021.
- Harris, R. and Baumann, I.: Open data policies and satellite Earth observation, *Space Policy*, Volume 32, pp. 44-53, ISSN 0265-9646, <https://doi.org/10.1016/j.spacepol.2015.01.001>, 2015.

- 970 Hashimoto, M., Nakajima, T., Dubovik, O., Campanelli, M., Che, H., Khatri, P., Takamura, T., and Pandithurai, G.: Development of a new data-processing method for SKYNET sky radiometer observations, *Atmos. Meas. Tech.*, *5*, 2723–2737, 2012.
- Hoffmann, R., Muttarak, R., Peisker, J. and Stanig, P.: Climate change experiences raise environmental concerns and promote Green voting. *Nat. Clim. Chang.* *12*, 148–155, <https://doi.org/10.1038/s41558-021-01263-8>, 2022.
- 975 Holben, B. N., Eck, T. F., Slutsker, I., Tanré, D., Buis, J. P., Setzer, A., Vermote, E., Reagan, J.A., Kaufman, Y., Nakajima, T., Lavenu, F., Jankowiak, I., and Smirnov, A.: AERONET — A federated instrument network and data archive for aerosol characterization, *Remote Sens. of Env.*, *66*, 1–16, 1998.
- Holzer-Popp, T., de Leeuw, G., Griesfeller, J., Martynenko, D., Klüser, L., Bevan, S., Davies, W., Ducos, F., Deuzé, J. L., Grainger, R. G., Heckel, A., von Hoyningen-Hüne, W., Kolmonen, P., Litvinov, P., North, P., Poulsen, C. A., Ramon, D., 980 Siddans, R., Sogacheva, L., Tanre, D., Thomas, G. E., Vountas, M., Descloitres, J., Griesfeller, J., Kinne, S., Schulz, M., and Pinnock, S.: Aerosol retrieval experiments in the ESA Aerosol_cci project, *Atmos. Meas. Tech.*, *6*, 1919–1957, <https://doi.org/10.5194/amt-6-1919-2013>, 2013.
- Ichoku, C., Chu, D. A., Chu, S., Kaufman, Y. J., Remer, L. A., Tanré, D., Slutsker, I., and Holben, B. N.: A spatio-temporal approach for global validation and analysis of MODIS aerosol products, *Geophys. Res. Lett.*, *29*(12), 8006, 985 [doi:10.1029/2001GL013206](https://doi.org/10.1029/2001GL013206), 2002.
- Julien, Y., and Sobrino, J.A.: NOAA-AVHRR Orbital Drift Correction: Validating Methods Using MSG-SEVIRI Data as a Benchmark Dataset. *Remote Sens.*, *13*, 925. <https://doi.org/10.3390/rs13050925>, 2021.
- Khaki, M., Hendricks Franssen, H.J., and Han, S.C.: Multi-mission satellite remote sensing data for improving land hydrological models via data assimilation. *Sci. Rep.* *10*, 18791, <https://doi.org/10.1038/s41598-020-75710-5>, 2020.
- 990 Kinne, S., D. O'Donnel, P. Stier, S. Kloster, K. Zhang, H. Schmidt, S. Rast, M. Giorgetta, T. F. Eck, and B. Stevens (2013): MAC-v1: A new global aerosol climatology for climate studies, *J. Adv. Model. Earth Syst.*, *5*, 704–740, [doi:10.1002/james.20035](https://doi.org/10.1002/james.20035).
- Koepke, P.: Effective Reflectance of Oceanic Whitecaps, *Applied Optics*, *23*(11), 1816–1824, 1984.
- Leiserowitz, A., Maibach, E., Rosenthal, S., Kotcher, J., Bergquist, P., Ballew, M., Goldberg, M., Gustafson, A., and Wang, 995 X.: Climate Change in the American Mind: April 2020. Yale University and George Mason University. New Haven, CT: Yale Program on Climate Change Communication. (<https://climatecommunication.yale.edu/publications/climate-change-in-the-american-mind-april-2020/>, last access 14 February 2022).
- Levy, R. C., Mattoo, S., Munchak, L. A., Remer, L. A., Sayer, A. M., Patadia, F., and Hsu, N. C.: The Collection 6 MODIS aerosol products over land and ocean, *Atmos. Meas. Tech.*, *6*, 2989–3034, <https://doi.org/10.5194/amt-6-2989-2013>, 2013.
- 1000 Loew, A., Bell, W., Brocca, L., Bulgín, C. E., Burdanowitz, J., Calbet, X., Donner, R. V., Ghent, D., Gruber, A., Kaminski, T., Kinzel, J., Klepp, C., Lambert, J.-C., Schaepman-Strub, G., Schröder, M., and Verhoelst, T.: Validation practices for satellite-based Earth observation data across communities, *Rev. Geophys.*, *55*, 779–817, <https://doi.org/10.1002/2017RG000562>, 2017.
- Meehl, G.A., Stocker, T. F., Collins, W. D., Friedlingstein, P., Gaye, A. T., Gregory, J. M., Kitoh, A., Knutti, R., Murphy, J. 1005 M., Noda, A., Raper, S. C. B., Watterson, I. G., Weaver, A. J., and Zhao, Z.-C.: Global Climate Projections. In: *Climate Change*

- 2007: The Physical Science Basis. Contribution of Working Group I to the Fourth Assessment Report of the Intergovernmental Panel on Climate Change. Cambridge University Press, Cambridge, U.K., 747-846, <https://www.ipcc.ch/report/ar4/wg1/> (last access 13 March 2022), 2007.
- 1010 Monahan, E.C. and O'Muircheartaigh, I.: Optimal power-law description of oceanic whitecap dependence on wind speed, *Journal of Physical Oceanography*, 10(12), 2094–2099, 1980.
- Morel, A.: Optical modeling of the upper ocean in relation to its biogenous matter content (case I waters), *J. Geoph. Res.*, 93(C9), 10749-10768, 1988.
- 1015 Morys, M., Mims III, F. M., Hagerup, S., Anderson, E., Baker, A., Kia, J., and Walkup, T.: Design, calibration, and performance of MICROTOPS II handheld ozone S. monitor and Sun photometer, *J. Geophys. Res.*, 106, 14,573–14,582, doi:10.1029/2001JD900103, 2001.
- North, P. R. J.: Estimation of aerosol opacity and land surface bidirectional reflectance from ATSR-2 dual-angle imagery: Operational method and validation, *J. Geophys. Res.*, 107, doi:10.1029/2000JD000,207, 2002.
- 1020 North, P.R.J., Brockmann, C., Fischer, J., Gomez-Chova, L., Grey, W., Heckle A., Moreno, J., Preusker, R. and Regner, P.: MERIS/AATSR synergy algorithms for cloud screening, aerosol retrieval and atmospheric correction. In Proc. 2nd MERIS/AATSR User Workshop, ESRIN, Frascati, 22- 26 September 2008. (CD-ROM), ESA SP-666, ESA Publications Division, European Space Agency, Noordwijk, The Netherlands, 2008.
- North, P., and Heckel, A.: AOD-SYN Algorithm Theoretical Basis Document, V 1.12, S3-L2-AOD-SYN-ATBD, https://sentinels.copernicus.eu/documents/247904/0/SYN_L2-3_ATBD.pdf/8dfd9043-5881-4b38-aae5-86fb9034a94d, 2019.
- Olbrich, P.: Open space: The global effort for open access to environmental satellite data. *Astropolitics*, 16, 230 – 236, 2018.
- 1025 Popp, T. , de Leeuw, G.; Bingen, C.; Brühl, C.; Capelle, V.; Chedin, A.; Clarisse, L.; Dubovik, O.; Grainger, R.; Griesfeller, J.; Heckel, A.; Kinne, S.; Klüser, L.; Kosmale, M.; Kolmonen, P.; Lelli, L.; Litvinov, P.; Mei, L.; North, P.; Pinnock, S.; Povey, A.; Robert, C.; Schulz, M.; Sogacheva, L.; Stebel, K.; Stein Zweers, D.; Thomas, G.; Tilstra, L.G.; Vandebussche, S.; Veefkind, P.; Vountas, M.; Xue, Y.: Development, Production and Evaluation of Aerosol Climate Data Records from European Satellite Observations (Aerosol_cci). *Remote Sensing*, 8(5), 421 doi:10.3390/rs8050421, 2016.
- 1030 Remer, L. A., Kaufman, Y. J., Tanré, D., Mattoo, S., Chu, D. A., Martins, J. V., Li, R.-R., Ichoku, C., Levy, R. C., Kleidman, R. G., Eck, T. F., Vermote, E., and Holben, B. N.: The MODIS Aerosol Algorithm, Products, and Validation, *J. Atmos. Sci.*, 62, 947–973, 2005.
- Remer, L. A., Mattoo, S., Levy, R. C., and Munchak, L. A.: MODIS 3 km aerosol product: algorithm and global perspective, *Atmos. Meas. Tech.*, 6, 1829–1844, <https://doi.org/10.5194/amt-6-1829-2013>, 2013.
- 1035 Sayer, A. M., Hsu, N. C., Bettenhausen, C., Ahmad, Z., Holben, B. N., Smirnov, A., Thomas, G. E., and Zhang, J.: SeaWiFS Ocean Aerosol Retrieval (SOAR): Algorithm, validation, and comparison with other data sets, *J. Geophys. Res.*, 117, D03206, <https://doi.org/10.1029/2011JD016599>, 2012a.
- 1040 Sayer, A. M., Hsu, N. C., Bettenhausen, C., Jeong, M.-J., Holben, B. N., and Zhang, J.: Global and regional evaluation of over-land spectral aerosol optical depth retrievals from SeaWiFS, *Atmos. Meas. Tech.*, 5, 1761–1778, <https://doi.org/10.5194/amt-5-1761-2012>, 2012b.

- Sayer, A. M., Hsu, N. C., Bettenhausen, C. and Jeong, M.-J.: Validation and uncertainty estimates for MODIS Collection 6 “Deep Blue” aerosol data, *J. Geophys. Res.*, 118, 7864–7872, doi:10.1002/jgrd.50600., 2013.
- 1045 Sayer, A. M., N. C. Hsu, J. Lee, W. V. Kim, O. Dubovik, S. T. Dutcher, D. Huang, P. Litvinov, A. Lyapustin, J. L. Tackett, and D. M. Winker: Validation of SOAR VIIRS over-water aerosol retrievals and context within the global satellite aerosol data record, *J. Geophys. Res.-Atmos.*, 123, 13496–13526, <https://doi.org/10.1029/2018JD029465>, 2018.
- Sayer, A. M., Hsu, N. C., Lee, J., Kim, W., and Dutcher, S.: Validation, stability, and consistency of MODIS Collection 6.1 and VIIRS Version 1 Deep Blue aerosol data over land, *J. Geophys. Res.-Atmos.*, 124, 4658–4688, <https://doi.org/10.1029/2018JD029598>, 2019.
- 1050 Sayer, A. M., Govaerts, Y., Kolmonen, P., Lipponen, A., Luffarelli, M., Mielonen, T., Patadia, F., Popp, T., Povey, A. C., Stebel, K., and Witek, M. L.: A review and framework for the evaluation of pixel-level uncertainty estimates in satellite aerosol remote sensing, *Atmos. Meas. Tech.*, 13, 373–404, <https://doi.org/10.5194/amt-13-373-2020>, 2020a.
- Shi, Y., Zhang, J., Reid, J. S., Hyer, E. J., and Hsu, N. C.: Critical evaluation of the MODIS Deep Blue aerosol optical depth product for data assimilation over North Africa, *Atmos. Meas. Tech.*, 6, 949–969, <https://doi.org/10.5194/amt-6-949-2013>, 2013
- 1055 Smirnov, A., B. N. Holben, I. Slutsker, D. M. Giles, C. R. McClain, T. F. Eck, S. M. Sakerin, A. Macke, P. Croot, G. Zibordi, P. K. Quinn, J. Sciare, S. Kinne, M. Harvey, T. J. Smyth, S. Piketh, T. Zielinski, A. Proshutinsky, J. I. Goes, N. B. Nelson, P. Larouche, V. F. Radionov, P. Goloub, K. Krishna Moorthy, R. Matarrese, E. J. Robertson, and F. Jourdin: Maritime Aerosol Network as a component of Aerosol Robotic Network, *J. Geophys. Res.*, 114, D06204, doi:10.1029/2008JD011257, 2009.
- 1060 Smirnov, A., Holben, B.N., Sakerin, S.M., Kabanov, D.M., Slutsker, I., Chin, M., Diehl, T.L., Remer, L.A., Kahn, R., Ignatov, A., Liu, L., Mishchenko, M., Eck, T.F., Kucsera, T.L., Giles, D. and Kopelevich, O.V.: Ship-Based Aerosol Optical Depth Measurements in the Atlantic Ocean: Comparison with Satellite Retrievals and Gocart Model. *Geophysical Research Letters*, 33, Article ID: L14817. <https://doi.org/10.1029/2006GL026051>, 2006.
- 1065 Smirnov, A., Holben, B. N., Giles, D. M., Slutsker, I., O'Neill, N. T., Eck, T. F., Macke, A., Croot, P., Courcoux, Y., Sakerin, S. M., Smyth, T. J., Zielinski, T., Zibordi, G., Goes, J. I., Harvey, M. J., Quinn, P. K., Nelson, N. B., Radionov, V. F., Duarte, C. M., Losno, R., Sciare, J., Voss, K. J., Kinne, S., Nalli, N. R., Joseph, E., Krishna Moorthy, K., Covert, D. S., Gulev, S. K., Milinevsky, G., Larouche, P., Belanger, S., Horne, E., Chin, M., Remer, L. A., Kahn, R. A., Reid, J. S., Schulz, M., Heald, C. L., Zhang, J., Lapina, K., Kleidman, R. G., Griesfeller, J., Gaitley, B. J., Tan, Q., and Diehl, T. L.: Maritime aerosol network as a component of AERONET – first results and comparison with global aerosol models and satellite retrievals, *Atmos. Meas. Tech.*, 4, 583–597, <https://doi.org/10.5194/amt-4-583-2011>, 2011.
- 1070 Sogacheva, L., Kolmonen, P., Virtanen, T. H., Rodriguez, E., Saponaro, G., and de Leeuw, G.: Post-processing to remove residual clouds from aerosol optical depth retrieved using the Advanced Along Track Scanning Radiometer, *Atmos. Meas. Tech.*, 10, 491–505, <https://doi.org/10.5194/amt-10-491-2017>, 2017.
- 1075 Sogacheva, L., de Leeuw, G., Rodriguez, E., Kolmonen, P., Georgoulias, A. K., Alexandri, G., Kourtidis, K., Proestakis, E., Marinou, E., Amiridis, V., Xue, Y., and van der A, R. J.: Spatial and seasonal variations of aerosols over China from two decades of multi-satellite observations – Part 1: ATSR (1995–2011) and MODIS C6.1 (2000–2017), *Atmos. Chem. Phys.*, 18, 11389–11407, <https://doi.org/10.5194/acp-18-11389-2018>, 2018a.
- Sogacheva, L., Rodriguez, E., Kolmonen, P., Virtanen, T. H., Saponaro, G., de Leeuw, G., Georgoulias, A. K., Alexandri, G., Kourtidis, K., and van der A, R. J.: Spatial and seasonal variations of aerosols over China from two decades of multi-satellite

1080 observations – Part 2: AOD time series for 1995–2017 combined from ATSR ADV and MODIS C6.1 and AOD tendency estimations, *Atmos. Chem. Phys.*, 18, 16631–16652, <https://doi.org/10.5194/acp-18-16631-2018>, 2018b.

Sogacheva, L., Popp, T., Sayer, A. M., Dubovik, O., Garay, M. J., Heckel, A., Hsu, N. C., Jethva, H., Kahn, R. A., Kolmonen, P., Kosmale, M., de Leeuw, G., Levy, R. C., Litvinov, P., Lyapustin, A., North, P., Torres, O., and Arola, A.: Merging regional and global aerosol optical depth records from major available satellite products, *Atmos. Chem. Phys.*, 20, 2031–2056, <https://doi.org/10.5194/acp-20-2031-2020>, 2020.

1085 Takamura, T., and Nakajima, T.: Overview of SKYNET and its activities, *Opt. Pura Apl.* 37, 3303-3308, 2004.

Wei, J., Li, Z. Q., Peng, Y. R., & Sun, L.: MODIS Collection 6.1 aerosol optical depth products over land and ocean: Validation and comparison. *Atmospheric Environment*, 201, 428– 440. <https://doi.org/10.1016/j.atmosenv.2018.12.004>, 2019.